A&A 553, A24 (2013)
DOI: 10.1051/0004-6361/201220558

Astronomy & Astrophysics

Populations of rotating stars

I. Models from 1.7 to 15 $M_\odot$ at Z = 0.014, 0.006, and 0.002 with $\Omega/\Omega_{\rm crit}$ between 0 and 1⋆,⋆⋆

C. Georgy[1,2], S. Ekström[3], A. Granada[3], G. Meynet[3], N. Mowlavi[3], P. Eggenberger[3], and A. Maeder[3]

[1] Astrophysics group, EPSAM, Keele University, Lennard-Jones Labs, Keele, ST5 5BG, UK
e-mail: c.georgy@keele.ac.uk
[2] Centre de Recherche Astrophysique de Lyon, École Normale Supérieure de Lyon, 46 allée d'Italie, 69384 Lyon Cedex 07, France
[3] Geneva Observatory, University of Geneva, Maillettes 51, 1290 Sauverny, Switzerland

Received 15 October 2012 / Accepted 20 February 2013

ABSTRACT

Context. B-type stars are known to rotate at various velocities, including very fast rotators near the critical velocity as the Be stars.
Aims. In this paper, we provide stellar models covering the mass range between 1.7 to 15 $M_\odot$, which includes the typical mass of known Be stars, at Z = 0.014, 0.006, and 0.002 and for an extended range of initial velocities on the zero-age main sequence.
Methods. We used the Geneva stellar-evolution code, including the effects of shellular rotation, with a numerical treatment that has been improved so the code can precisely track the variation in the angular momentum content of the star as it changes under the influence of radiative winds and/or mechanical mass loss.
Results. We discuss the impact of the initial rotation rate on the tracks in the Hertzsprung-Russell diagram, the main-sequence (MS) lifetimes, the evolution of the surface rotation and abundances, as well as on the ejected masses of various isotopes. Among the new results obtained from the present grid we find that 1) fast-rotating stars with initial masses around 1.7 $M_\odot$ present at the beginning of the core hydrogen-burning phase quite small convective cores with respect to their slowly rotating counterparts. This fact may be interesting to keep in mind in the framework of the asteroseismic studies of such stars. 2) The contrast between the core and surface angular velocity is higher in slower rotating stars. Our results are in agreement with the very few values obtained for B-type stars from asteroseismology. 3) At Z = 0.002, the stars in the mass range of 1.7 to 3 $M_\odot$ with a mean velocity on the MS of the order of 150 km s^{-1} show N/H enhancement superior to 0.2 dex at mid-MS, and superior to 0.4 dex at the end of the MS phase. At solar metallicity the corresponding values are below 0.2 dex at any time in the MS.
Conclusions. An extended database of stellar models containing 270 evolutionary tracks is provided to the community.

Key words. stars: general – stars: evolution – stars: rotation – stars: emission-line, Be – stars: mass-loss

1. Introduction

In the framework of the new grids of stellar models that the Geneva stellar evolution group has recently made available to the community (Ekström et al. 2012, hereafter Grids I), we propose a more detailed study of some subsamples of the full grids, offering a reduced mass range, but a more extended coverage in initial rotation rates.

An interesting subsample is the mass domain between 1.7 to 15 $M_\odot$, which corresponds roughly to the domain of the early A- and B-type stars. This range of mass covers the transition from the massive and energetic O-stars, dominated by their stellar winds, to the less massive A stars with negligible winds. Then, in the B-type star range, the interplay between stellar winds and rotation will together affect the evolution of the star and the injection of mass and energy to the circumstellar environment, and also determine the post-main-sequence (post-MS) fate of the star. Moreover, this range contains the interesting case of Be-type stars. Since rapid rotation and reaching the critical velocity is thought at least partially to be involved to explain the Be-star phenomenon (Martayan et al. 2007, 2010), we provide in this grid an extended coverage of initial rotations up to the fastest cases.

Previous studies have already explored the evolution of B stars towards the critical velocity as a function of the metallicity (Ekström et al. 2008). However, the Geneva stellar-evolution code at that time could not follow the model through a critical-rotation phase while keeping precise track of the stellar angular-momentum content, and computation of the models was stopped when they reached the beginning of that stage. Several recent improvements in the Geneva code now make it possible to compute models of critically rotating stars, and to give a theoretical estimation of the equatorial mass loss that such stars undergo during this phase. In that context, we performed a new analysis of stars in the range of 1.7 to 15 $M_\odot$ at various metallicities: Z = 0.014 (solar), Z = 0.006 (LMC), and Z = 0.002 (SMC), with initial rotation rates on the zero-age main sequence (ZAMS) between $0 < \Omega/\Omega_{\rm crit} < 0.95$.

The present theoretical database will allow synthetic clusters to be built with the inclusion of any distribution of initial rotational velocities. In a forthcoming paper, we shall discuss our population-synthesis code and compare the results with observed stellar clusters and field star populations.

⋆ Tables 2–4 and Figs. 11, 12 are available in electronic form at http://www.aanda.org

⋆⋆ The model tables are only available in electronic form at the CDS via anonymous ftp to cdsarc.u-strasbg.fr (130.79.128.5) or via http://cdsarc.u-strasbg.fr/viz-bin/qcat?J/A+A/553/A24

This paper is organised as follows. In Sect. 2, we briefly recall the effect of the rotation on the stellar surface properties. We explain the numerical method used to estimate the equatorial mass loss for critically rotating stars. In Sect. 3, we briefly describe the parameters and the physical ingredients used to perform our numerical simulations. The results are presented in Sect. 4. Some aspects of the advanced phases are discussed in Sect. 5. Finally, Sect. 6 contains our conclusions.

A complete discussion concerning our faster rotating models and comparison with observations of Be-type stars is the subject of the second paper of this series (Granada et al. 2013, hereafter Paper II).

2. Angular momentum losses due to stellar winds and equatorial mechanical mass losses: numerical method

2.1. Recall of the effects of rotation on the properties of the stellar surface

Rotation strongly affects the stellar surface in several ways. First of all, the shape of the surface itself is modified: the equatorial radius becoming larger than the polar one under the action of the centrifugal force. The shape of the star depends on several parameters (ratio to the critical velocity, latitudinal differential rotation, etc., see Zorec et al. 2011). Here, given the shellular hypothesis used in our stellar-evolution code (see Grids I, for details) the shape of the star is accounted for in the framework of the Roche model, as it allows for a quick numerical treatment. In this context, the only pertinent parameter for describing the stellar surface is the ratio of the actual angular velocity to the critical one $\omega = \Omega/\Omega_{\rm crit}$ (see e.g. Georgy et al. 2011). The parameter $\Omega_{\rm crit}$ is defined as

$$\Omega_{\rm crit} = \sqrt{\frac{GM}{R^3_{\rm e,\,crit}}}, \tag{1}$$

with $R_{\rm e,\,crit}$ the equatorial radius when the star rotates at the angular velocity $\Omega_{\rm crit}$. In the framework of this model, the maximum ratio of the equatorial-to-polar radius (when $\Omega = \Omega_{\rm crit}$) is 1.5. This is observationally supported by the observations of the fast-rotating star Achernar (Vinicius et al. 2006; Carciofi et al. 2008).

According to Maeder & Meynet (2000), the total acceleration at the surface of a rotating star, including gravity, radiation-pressure acceleration and centrifugal acceleration can be expressed as (vectors are in boldface)

$$\boldsymbol{g}_{\rm tot} = \boldsymbol{g}_{\rm eff}\,(1 - \Gamma(\Omega, \theta))\,, \tag{2}$$

with $\boldsymbol{g}_{\rm eff} = \boldsymbol{g}_{\rm grav} + \boldsymbol{g}_{\rm cen}$ the sum of the gravitational and centrifugal accelerations, and $\Gamma(\Omega, \theta)$ the local Eddington factor, accounting for the effects of the rotation. Following Maeder & Meynet (2000), we define a velocity that vanishes the expression (2) as a critical velocity. The first critical velocity is given by $\boldsymbol{g}_{\rm eff} = 0$, and can be expressed as

$$v_{\rm crit,\,1} = \sqrt{\frac{2}{3}\frac{GM}{R_{\rm p,\,crit}}}, \tag{3}$$

with $R_{\rm p,\,crit}$ being the polar radius when the star reaches $\Omega_{\rm crit}$. The second critical velocity is reached when $1 - \Gamma(\Omega, \theta) = 0$. It is only possible for stars with a very high Eddington factor ($\Gamma_{\rm Edd} \gtrsim 0.639$). In this work, all the considered stellar models remain far from this value, and the only pertinent critical velocity to consider is the first one. In the following text, we systematically use the term "critical velocity" for "first critical velocity".

Rotation not only affects the shape of the surface, but also produces latitudinal variations in the radiative flux, effective temperature, and mass flux, producing an anisotropic stellar wind (see e.g. Maeder & Meynet 2000; Maeder 2002). The effects of such a wind on the evolution of stars remaining far from the critical velocity (which is the case for most of stars) are moderate (Georgy et al. 2011), and can usually be neglected. In this paper, however, some of our models evolve very close to or even at the critical velocity. The effects of anisotropic winds are thus stronger (more than 10% in terms of angular-momentum loss compared to models where such effects are neglected, see Georgy et al. 2011), and are accounted for in this work. Also, wind anisotropies may produce, at least for some periods, non-spherical shape bubbles around rapidly rotating stars, a feature that may be interesting for comparisons with observations.

2.2. Computation of the equatorial mechanical mass loss

During the stellar lifetime, both the surface angular velocity and the critical one evolve, making the rotation rate $\omega = \Omega_{\rm surf}/\Omega_{\rm crit}$ change as a function of time. It is thus possible for a star to reach the critical velocity during its life, even if it started on the ZAMS with $\omega_{\rm ini} < 1$. Once this limit is attained, the effective gravity at the equator of the star is nil. We thus expect a strong enhancement of the mass loss in the equatorial region, hereafter called "mechanical mass loss", which removes the overcritical layers and maintains the surface at the critical velocity or slightly below. The exact details of this process is to date not well known, and would need complex simulations that combine hydrodynamics and radiative transfer. It is currently not possible to perform such computations coupled with a stellar-evolution code for the full duration of the stellar life.

To account for this mechanical mass loss in our stellar-evolution code, we proceed as follows[1]: we estimate the angular-momentum amount $\Delta\mathcal{L}_{\rm rad}$ that the model loses through radiative stellar winds during a time step, on the basis of the estimated surface quantities (radius, mass-loss rate, etc.). If the effects of the anisotropic stellar winds are not accounted for, we have

$$\Delta\mathcal{L}_{\rm rad} = \frac{2}{3}\Delta M_{\rm rad}\Omega_{\rm surf}r^2_{\rm surf}, \tag{4}$$

with $\Delta M_{\rm rad}$ the total amount of mass lost during the time step due to radiative stellar winds, and $r_{\rm surf}$ the radius of the star. (This mean radius is defined as the radius that would have a spherical star having the same luminosity and effective temperature.) If the wind anisotropy is accounted for, this expression is more complex and needs a numerical integration over the stellar surface (see Georgy et al. 2011).

Knowing the initial characteristics of the model at the beginning of the time step, we have to estimate whether the radiative mass loss is sufficient to keep the star below the critical velocity at the end of the time step. Moreover, because of numerical difficulties, it is not possible to maintain the model exactly at the critical velocity. We thus define a maximal ratio $\omega_{\rm max} \equiv \frac{\Omega_{\rm max\ allowed}}{\Omega_{\rm crit}}$. In our computations, it is set to $\omega_{\rm max} = 0.99$.

At any time, the structure of our numerical model is composed of an envelope, where convection is non-adiabatic and ionisation not complete, and of an interior zone where convection is

[1] This approach is similar to the one described in Grids I ensuring the conservation of angular momentum.

adiabatic and ionisation complete. The envelope, which encompasses a very small fraction of the total mass, typically one ten-thousandth, is assumed to rotate with the same angular velocity as the uppermost layers of the interior zone[2]. The mass removed by the mass loss will be a fraction of the mass of the envelope. The removal of these layers will remove angular momentum and a new angular velocity distribution inside the star will be built up so that the total angular momentum of the star will be decreased by the exact amount lost by the star. Since angular momentum can be transported over a given distance in a time step, the zone where Ω is modified covers a zone with a depth approximately equal to the radial component of the meridional current multiplied by the time step. We thus have to compute the correcting factors of Ω in that zone so that the process keeps precise track of the angular momentum. In the following, we denote $N_{\rm corr}$ as the number of layers that are affected by the mass loss. To estimate the correcting factors, called q below, we suppose that:

- the changes in the structure of the star are small enough during the time step considered that they can be neglected for computing the q values;
- the angular momentum removed by the radiative stellar wind is equally removed from the envelope and the first $N_{\rm corr}$ layers (see Georgy 2010 and Grids I for more details). That means that q is constant over the whole zone where Ω will be affected by the mass loss, or that $\Omega_{\rm i,\,new} = \Omega_{\rm i,\,ini}\,(1+q)$, with i the number of the shell considered;
- no other angular momentum transport mechanisms act during the time step.

The initial angular momentum content of the $N_{\rm corr}$ layers is $\mathcal{L}_{\rm tot,\,ini} = \mathcal{L}_{\rm e,\,ini} + \sum_{i=1}^{N_{\rm corr}} \mathcal{L}_{i,\,\rm ini}$, where the subscript "e" is for the envelope, and i concerns the ith layers below the surface. Assuming that the mass carried away by the stellar winds is removed in the envelope, we can thus write the estimated total amount of angular momentum in the $N_{\rm corr}$ layers after the mass loss occurred as

$$\mathcal{L}_{\rm tot,\,fin} = \mathcal{L}_{\rm e,\,ini}\,(1+q)\left(1-\frac{\Delta M_{\rm rad}}{m_{\rm e,\,ini}}\right) + (1+q)\sum_{i=1}^{N_{\rm corr}}\mathcal{L}_{i,\,\rm ini}, \tag{5}$$

with $m_{\rm e,\,ini}$ the mass of the envelope at the beginning of the time step. Finally, since we must have $\mathcal{L}_{\rm tot,\,fin} = \mathcal{L}_{\rm tot,\,ini} - \Delta\mathcal{L}_{\rm rad}$, we obtain

$$q = \frac{\mathcal{L}_{\rm e,\,ini}\frac{\Delta M_{\rm rad}}{m_{\rm e,\,ini}} - \Delta\mathcal{L}_{\rm rad}}{\mathcal{L}_{\rm tot,\,ini} - \mathcal{L}_{\rm e,\,ini}\frac{\Delta M_{\rm rad}}{m_{\rm e,\,ini}}}. \tag{6}$$

Knowing q, it is now possible to estimate the surface angular velocity $\Omega_{\rm surf,\,new}$ at the end of the time step. If $\Omega_{\rm surf,\,new} < \Omega_{\rm max\ allowed}$, the model does not need to lose more angular momentum and the angular momentum losses estimate is complete.

If $\Omega_{\rm surf,\,new} > \Omega_{\rm max\ allowed}$, the radiative mass loss is not strong enough to maintain the star below the critical velocity, and other expressions for $\mathcal{L}_{\rm tot,\,fin}$ and q have to be obtained. In contrast to previous case, where the mass loss rate imposes an angular momentum loss, we need here to remove an excess of angular momentum, and this will determine an additional mass loss.

[2] Note that during the red (super)giant phase, the envelope is much bigger than during the MS. When the star crosses the Hertzsprung-Russell diagram and becomes red, the mass-coordinate of the base of the envelope is progressively decreased, up to $M_r/M_{\rm tot} = 0.98$.

We assume that this additional mass, $\Delta M_{\rm mech}$, is lost mechanically at the equator, and rotates at the same angular velocity as the surface. It thus removes the following angular momentum:

$$\Delta\mathcal{L}_{\rm mech} = \Delta M_{\rm mech}\Omega_{\rm surf} r_{\rm eq}^2, \tag{7}$$

with $r_{\rm eq}$ the equatorial radius. The mechanical mass loss has to bring the angular velocity of the stellar surface down to $\Omega_{\rm max\ allowed}$. We thus define the factor $q_{\rm lim}$ as $\Omega_{\rm surf,\,new} = \Omega_{\rm max\ allowed} = \Omega_{\rm surf,\,ini}\,(1+q_{\rm lim})$, and the new angular velocity of each layer where the correction is applied becomes

$$\Omega_{i,\,\rm new} = \Omega_{i,\,\rm ini}\,(1+q_{\rm lim}) = \Omega_{i,\,\rm ini}\frac{\Omega_{\rm max\ allowed}}{\Omega_{\rm surf,\,ini}}. \tag{8}$$

As before, we assume that the effect of the mechanical mass loss will affect $N_{\rm corr}$ layers below the surface. The angular momentum of the star that is needed to have a sub-critically rotating surface at the end of the time step is estimated to be

$$\mathcal{L}_{\rm tot,\,lim} = \mathcal{L}_{\rm e,\,ini}\,(1+q_{\rm lim})\left(1-\frac{\Delta M_{\rm rad}+\Delta M_{\rm mech}}{m_{\rm e,\,ini}}\right) + (1+q_{\rm lim})\sum_{i=1}^{N_{\rm corr}}\mathcal{L}_{i,\,\rm ini}. \tag{9}$$

Knowing that $\mathcal{L}_{\rm tot,\,lim} = \mathcal{L}_{\rm tot,\,ini} - \Delta\mathcal{L}_{\rm rad} - \Delta\mathcal{L}_{\rm mech}$, and using relations (7) and (8), the mechanical mass lost during the time step $\Delta M_{\rm mech}$, which is the only unknown of the equations, can now be defined as

$$\Delta M_{\rm mech} = \frac{\mathcal{L}_{\rm tot,\,ini}\left(1-\frac{\Omega_{\rm max}}{\Omega_{\rm surf,\,ini}}\right) + \mathcal{L}_{\rm e,\,ini}\frac{\Delta M_{\rm rad}}{m_{\rm e,\,ini}}\frac{\Omega_{\rm max}}{\Omega_{\rm surf,\,ini}} - \Delta\mathcal{L}_{\rm rad}}{\Omega_{\rm surf,\,ini}r_{\rm eq}^2 - \frac{\mathcal{L}_{\rm e,\,ini}}{m_{\rm e,\,ini}}\frac{\Omega_{\rm max}}{\Omega_{\rm surf,\,ini}}}, \tag{10}$$

providing an estimation on how much mass should be removed from the equator of the star in order to keep the star below the critical velocity. This mass will probably form an equatorial circumstellar disc. In this paper, we assume that this mass is lost, and is not re-accreted on the star.

As in Grids I, $N_{\rm corr}$ is set to 200 in this work. This value ensures that during a characteristic time step, the diffusion and the advection of the angular momentum affect at least these layers. To avoid a strong discontinuity at the edge of the zone where the correction is applied, we limited the time step in order to limit the value of q to 0.005 (0.01 for models rotating with $\omega < 0.2$). Moreover, during the red (super)giant phase, during which a large surface convective zone develops, the correction is applied only to the whole convective zone, as soon as it stretches over more than 50 layers.

The above method for computing the variation in Ω due to the mass loss, while allowing the conservation of the angular momentum, is probably quite schematic, especially for what concerns the equatorial mass loss when the surface velocity becomes overcritical. Among the limitations, we can mention that the process that ultimately pushes the matter out is absent. This process can be momentum input by radiation and/or pulsations and/or convection. To fully describe such processes, other tools than the present stellar-evolution code are necessary. The discussion about to what extent the results of the present models depend on the computational time step and on the value of $\omega_{\rm max}$ is presented in Paper II.

3. Physics of the models

3.1. General context

The physical ingredients included in our models are the same as in Grids I, except for the following points:

- Contrary to Grids I, some of the models presented in the present paper evolve for a significant time near the critical velocity. To follow the evolution of the surface velocities as best as possible, as well as the total angular momentum content, the effect of anisotropic winds are accounted for as in Georgy et al. (2011).
- Some of our models reach the critical velocity during their evolution. In that case, the mechanical equatorial mass loss is accounted for as described above.

Our grid of models contains ten different masses (1.7, 2.0, 2.5, 3.0, 4.0, 5.0, 7.0, 9.0, 12.0 and 15.0 $M_{\odot}$), with nine different initial rotation rates (ω = 0, 0.1, 0.3, 0.5, 0.6, 0.7, 0.8, 0.9, 0.95), and this for three different metallicities: Z = 0.014 (solar metallicity), Z = 0.006 (Large Magellanic Cloud metallicity) and Z = 0.002 (Small Magellanic Cloud metallicity). This grid thus covers a mass range centred on the B-type stars[3]. The models are evolved up to the helium flash ($M_{\rm ini} \leq 2\,M_{\odot}$), the early asymptotic giant branch ($2.5\,M_{\odot} \leq M_{\rm ini} \lesssim 9\,M_{\odot}$) or the end of central carbon burning ($M_{\rm ini} \gtrsim 9\,M_{\odot}$).

For the non-solar metallicities, the initial abundances are set as follows

- The hydrogen and helium abundances are computed assuming that they vary linearly with respect to the total metal content Z from the values given by the Big Bang nucleosynthesis to the present values. We thus have:

$$Y(Z) = Y_{\rm P} + \frac{\Delta Y}{\Delta Z} Z, \tag{11}$$

  with $Y_{\rm P}$ = 0.2484 the primordial helium abundance (Cyburt et al. 2003), and $\Delta Y/\Delta Z$ = 1.257. The hydrogen mass fraction is given by $X = 1 - Y - Z$.
- The relative abundances of all other chemical species are the solar ones (the abundances are only scaled on a lower total metal content).

3.2. Note on the diffusion coefficients and the calibrations

Stellar evolution computations with one-dimensional codes such as those presented in this paper account for physical processes that are not unidimensional (convection, rotation, turbulent mixing, etc.). One accounts for these effects through simplified theories, which have various free parameters that have to be calibrated on observations: overshoot parameter, mixing length, and shear mixing efficiency. Moreover, the implementation of the rotation includes two diffusion coefficients: the horizontal one $D_{\rm h}$ and the shear one $D_{\rm shear}$. In the literature, there are three different expressions for $D_{\rm h}$ (Zahn 1992; Maeder 2003; Mathis et al. 2004) and two for $D_{\rm shear}$ (Maeder 1997; Talon & Zahn 1997). Combining them allows for six different implementations of the rotation, and there is to date no reason to prefer any one of them on the basis of theoretical considerations.

The calibration of the overshoot parameter and of the mixing length is detailed in Grids I. In the framework of this paper, we add some complementary details on the choice and the calibration of the diffusion coefficients related to the rotation. In this work, as well as in Grids I, we chose $D_{\rm h}$ as in Zahn (1992) and $D_{\rm shear}$ as in Maeder (1997). This choice relies mainly on it is allowing the following two behaviours simultaneously:

- The rotating models with an initial rotational velocity that we assume to be the more representative ($v_{\rm eq,\,ini}/v_{\rm crit}$ = 0.4, based on the work of Huang & Gies 2006, see also Grids I for more details) have a blue loop in the mass range ~5–~9 $M_{\odot}$;
- The mixing at the edge of the convective core during the MS is strong enough, leading to a bigger core than in the non-rotating case. This allows rotation to increase the size of the convective core in agreement with recent asteroseismic observations by Neiner et al. (2012), who support the view that rotation enlarges the convective core.

The efficiency of the mixing (the $f_{\rm energ}$ factor in Eq. (4) in Grids I) was calibrated to reproduce typical chemical enrichments at the surface of solar-metallicity MS B-type stars for our assumed typical initial rotation velocity (the rotating models in Grids I, see their Fig. 11). To be consistent with the previous work, we kept the same value for all the models presented here.

3.3. Electronic data

All the electronic tables of these models are available at `http://obswww.unige.ch/Recherche/evol/-Database-`, as well as at the CDS. We have developed an interactive web application allowing for the downloading of a stellar model with given Z, M, and $\Omega/\Omega_{\rm crit}$ interpolated between the computed models presented here. It also offers isochrones computation at the desired age or age range. This application is available at `http://obswww.unige.ch/Recherche/evoldb/index/`. The database contains the models presented in this paper, as well as the models from Ekström et al. (2012) and Mowlavi et al. (2012). In the near future, it will be extended with additional metallicities.

4. Results

The overall characteristics at the end of the main burning stages for all our models are presented in Tables 2 to 4. General Hertzsprung-Russell diagrams (HRD) with a colour scale indicating ω are presented in Figs. 10 to 12. The shaded area represents the approximative position of the Cepheid instability strip, according to Tammann et al. (2003).

4.1. Mixing efficiency

In Fig. 3, we show, for two masses and two metallicities, the profile of the diffusion coefficients responsible for the transport of the chemical species: the effective diffusion coefficient $D_{\rm eff}$ accounting for the composed effects of the meridional circulation and of the strong horizontal turbulence (see Chaboyer & Zahn 1992), and the shear-mixing diffusion coefficient $D_{\rm shear}$, at roughly the middle of the MS phase ($X_{\rm H,\,cen}$ = 0.3). We see that except near the edge of the convective core, where $D_{\rm eff}$ dominates, the shear mixing is responsible for the transport of the chemical species in most of the radiative envelope. We see a clear trend to comparing the two different masses for the same metallicity: both $D_{\rm eff}$ and $D_{\rm shear}$ are higher for a higher initial mass. In contrast, the coefficients do not show any noticeable

[3] As in Paper II, we consider that a star is a B-type star if it has an effective temperature such as 10 000 K < $T_{\rm eff}$ < 30 000 K.

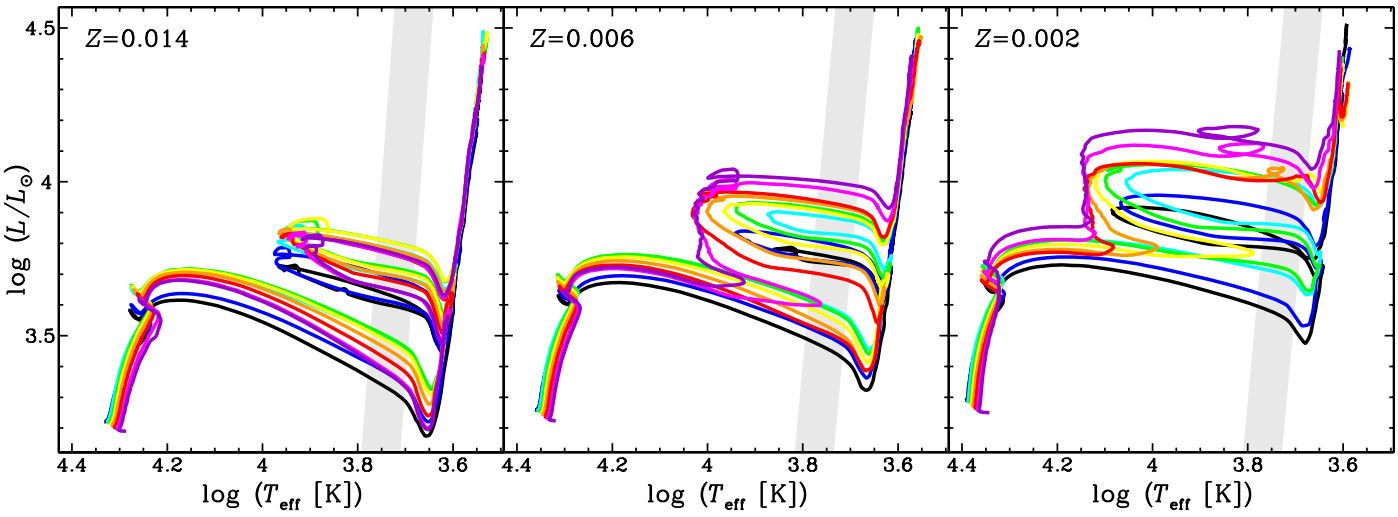

Fig. 1. HRD for the 7 $M_\odot$ models with $\omega_{\rm ini} = \Omega_{\rm ini}/\Omega_{\rm crit}$ = 0 (black), 0.1 (blue), 0.3 (cyan), 0.5 (green), 0.6 (yellow), 0.7 (orange), 0.8 (red), 0.9 (magenta), and 0.95 (purple). Models at Z = 0.014 (*left*), Z = 0.006 (*centre*), and Z = 0.002 (*right*).

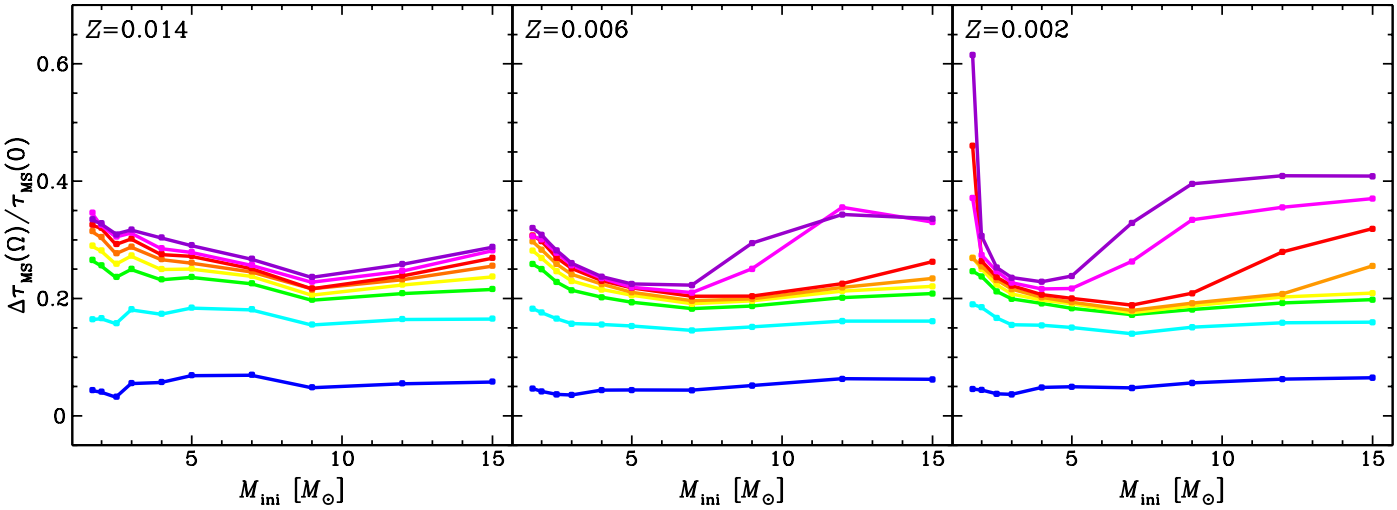

Fig. 2. MS lifetime enhancement as a function of the initial mass for all the models (same colour code as in Fig. 1). Models at Z = 0.014 (*left*), Z = 0.006 (*centre*), and Z = 0.002 (*right*).

difference with respect to the metallicity. However, due to the lower opacities at lower metallicity, low-Z stars are more compact, leading to a shorter characteristic timescale for the diffusion ($\tau_{\rm diff} \sim \frac{R^2}{D}$), and thus a more efficient enrichment of the surface (see the discussion in Sect. 4.5). This behaviour remains true for all the models at the three considered metallicities.

4.2. HRD, lifetimes

As described by Meynet & Maeder (2000) and Ekström et al. (2008), the position on the ZAMS is governed by the centrifugal force: rotating models behave like lower mass ones, with a shift in the tracks toward lower L and $T_{\rm eff}$. When the evolution proceeds, rotational mixing brings fresh hydrogen into the core, slowing down its decrease in mass. Also, newly produced helium is brought into the radiative zone, so the model evolves on a bluer and more luminous track.

As shown in Fig. 1, the luminosity attained at the end of the MS, and thus during the crossing of the Hertzsprung-Russell gap, increases with the rotation rate up to $\omega_{\rm ini} \leq 0.5$. Beyond, the luminosity decreases again and the crossing occurs at a luminosity that is lower than the one of the $\omega_{\rm ini}$ = 0.3 model, except at Z = 0.002, where the luminosity at the end of the MS increases again above $\omega_{\rm ini} \sim 0.8$. This behaviour is directly related to the size of the convective core, which governs the luminosity at the end of the MS. During the MS, the evolution of the size of the convective core relies on two counteracting physical processes linked to rotation. First, rotation generates an additional support against gravity due to the centrifugal force. These effects tend to decrease the size of the core and its luminosity. Second, the rotational mixing at the edge of the core progressively brings fresh material into the core, increasing its mass, hence its luminosity. Both effects are responsible for the non-monotonic behaviour of the luminosity at the HRD-crossing as a function of the initial rotation rate.

For the models going through a blue loop during core He-burning (passing through a classical Cepheid phase), we note that rotation increases the luminosity at which the loop occurs. The effect of rotation on the blue loops becomes spectacular at low metallicity, with the disappearance of the typical loop pattern for the most rapid rotators. We discuss this point in more detail in Sect. 5.1.

Rotational mixing increases the MS lifetimes, as shown in Fig. 2. At solar metallicity, for the mass range considered, the

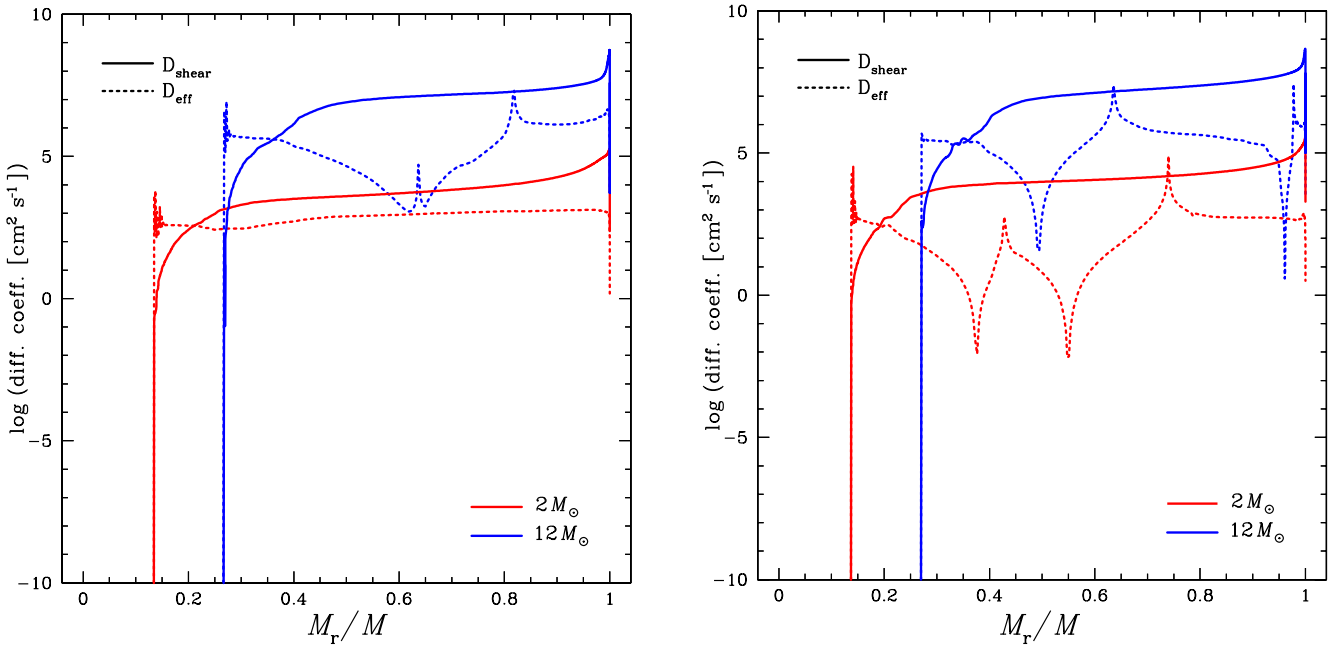

Fig. 3. Diffusion coefficients profiles for a 2 (red curves) and a 12 $M_\odot$ model (blue curves) at $Z = Z_\odot$ *(left panel)* and $Z = Z_{\rm SMC}$ *(right panel)*. The effective diffusion coefficient $D_{\rm eff}$ (accounting for the effects of the meridional circulation on the chemical species) is plotted in dashed lines, and the shear mixing diffusion coefficient in solid lines.

increase does not much vary as a function of the initial mass. It amounts to about 15–25% for $\omega_{\rm ini}$ between 0.30 and 0.50. For the most rapid rotators considered here, it may reach values as high as 30–35%.

When the metallicity decreases, the variation with the initial mass becomes more marked at the low and high mass ranges considered. As a numerical example, at $Z = 0.002$, the maximum increase reaches values as high as 62% for the 1.7 $M_\odot$ and as high as 41% for the 15 $M_\odot$.

The high sensitivity at 1.7 $M_\odot$ comes from the central temperature at the beginning of the core H-burning phase being around 20 MK, i.e. in the range of temperature at which CNO-burning begins to dominate the pp-chain for the energy production. When rotation is fast enough, the hydrostatic effects of rotation decrease the central temperature, and therefore the pp-chain becomes the dominant energy production channel. Typically, at 200 Myr, the three more rapidly rotating models have $T_{\rm c} < 21.4$ MK, while all the others have $T_{\rm c} > 21.7$ MK. As a result, the convective core is smaller during the first part of the MS phase (see Fig. 5, left)[4]. It is amazing to note that such a slight difference in $T_{\rm c}$ is enough to pass from pp-chain to CNO-cycle dominated energy production. When evolution proceeds, and the central temperature increases, the convective core grows and reaches values even higher than the values obtained at the beginning of the core H-burning phase in the non-rotating model.

At low metallicities and masses above 5–7 $M_\odot$, we obtain large increases of the MS lifetimes for $\omega_{\rm ini} > 0.70$. Actually, some small convective zones develop in the region above the core, where there is a variable chemical composition. (This phenomenon is related to the phenomenon of "semi-convection".) These convective zones mix the region above the core (and, in some cases, even merge with the core), bringing fresh hydrogen close to it, favouring a refuelling of the core, and in turn increasing the lifetime on the MS. The details in the development of these intermediate convective zones are very sensitive to the precise prescription used for rotation, however the general features seem robust and occur independently of the physical ingredients.

In Fig. 4, we compare the degree of dispersion of the MS lifetimes due to change of metallicity and of rotation for two initial masses. We see that for the 15 $M_\odot$ (Fig. 4, right), up to $\omega_{\rm ini} = 0.60$, the dispersion due to rotation is much greater than the one due to metallicity. This is due to the change in metallicity for the hot massive stars that have only moderate effects on the opacities[5], hence on the luminosity of the stars. In that case, the mixing is the dominant effect changing the MS duration. At high velocities, however, the change brought by varying the metallicity are more important, but this is again a consequence of rotational mixing whose consequences are not the same depending on the initial metallicity (see above).

In the low mass-range (1.7 $M_\odot$, Fig. 4, left), we somehow have an inverse situation, in the sense that, in general, the effects of changing the metallicity have a greater impact on the MS lifetime than changing the initial velocity. This reflects the fact that, on the one hand, rotational mixing becomes less efficient in low-mass stars (see Fig. 8), and on the other hand, the impact of a change in Z on the opacity is much greater than in the higher mass range.

4.3. Core mass vs. rotation and metallicity

As mentioned above, the additional support against gravity produced by the rotation allows the central temperatures to be lower for increasing initial velocities. This implies that the size of the convective core on the ZAMS decreases as a function of

[4] The decrease shown in Fig. 5 (left) is of the same order of magnitude as the one obtained by Mowlavi et al. (2012) when the initial mass decreases from 1.7 down to 1.6 $M_\odot$, precisely for the same effect as on the energy production channel.

[5] The opacity in the temperature range of the massive stars is dominated by electron scattering, which is only marginally affected by a change in the chemical composition.

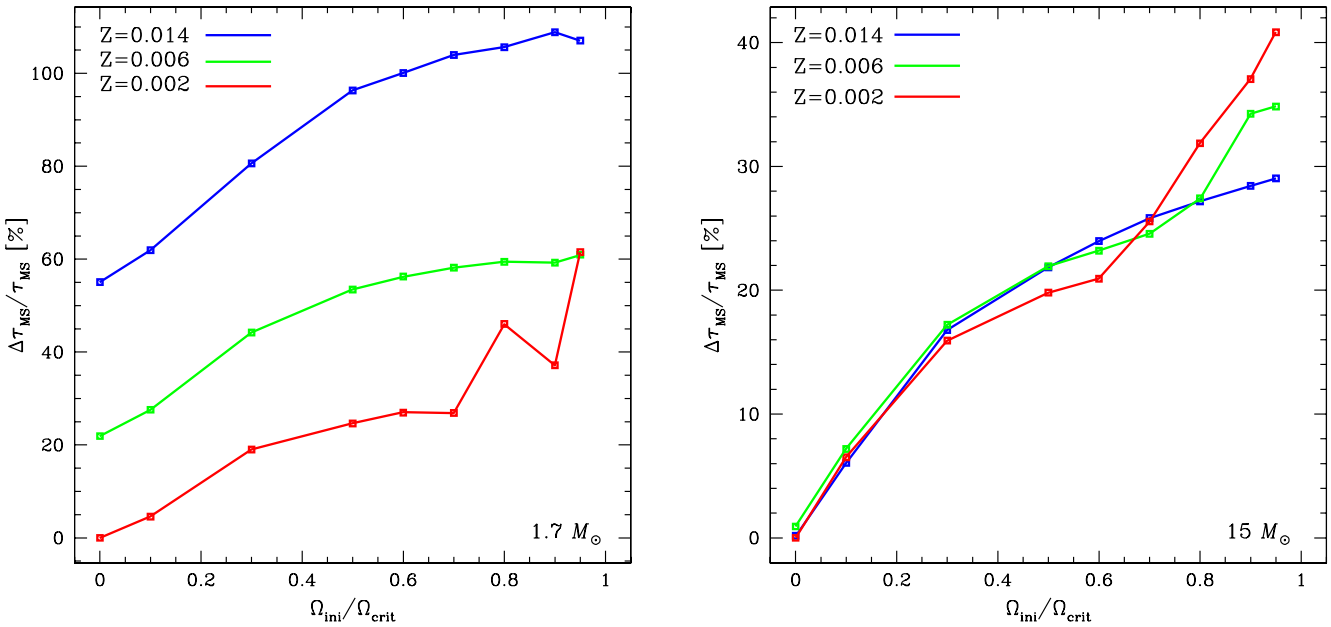

Fig. 4. MS duration enhancement as a function of the initial rotation rate. *Left*: 1.7 $M_\odot$ models. *Right*: 15 $M_\odot$ models.

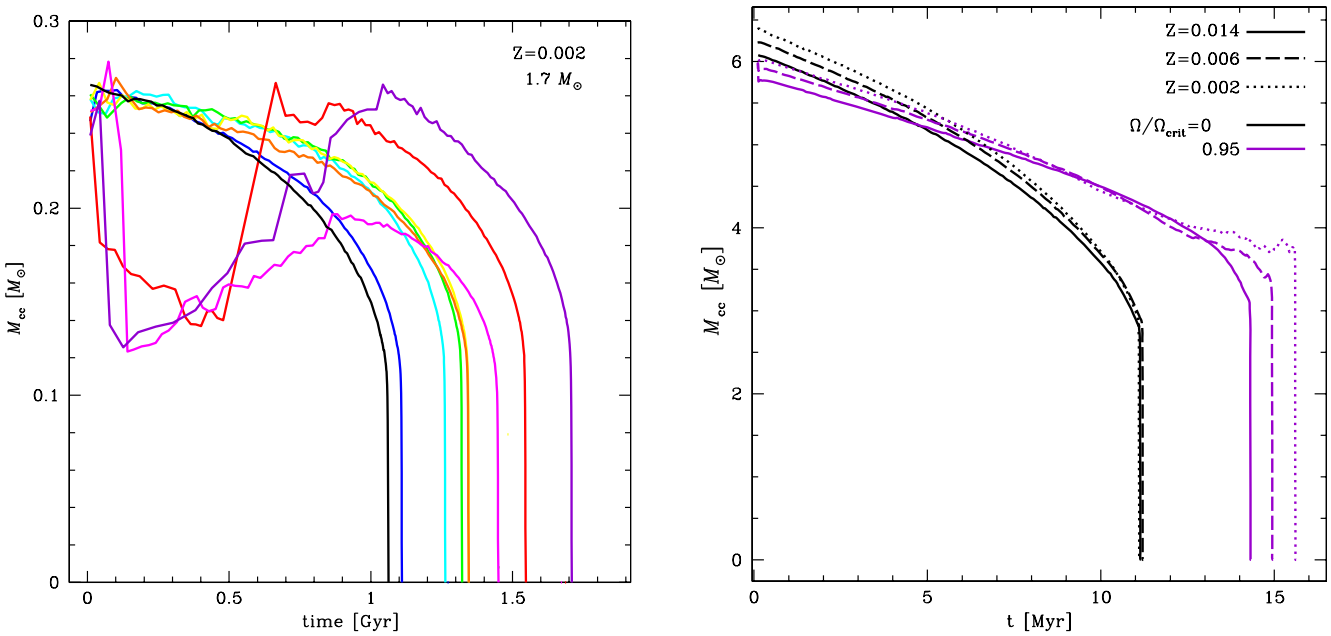

Fig. 5. Core mass evolution. *Left*: 1.7 $M_\odot$ models at $Z = 0.002$ (same colour code as in Fig. 1). *Right*: 15 $M_\odot$ models at the three Z, and $\Omega/\Omega_{crit} = 0$ and 0.95.

the initial rotation velocity. However, as evolution proceeds, the more efficient mixing in the more rapidly rotating stars increases the size of the convective core, which becomes bigger than the core of more slowly rotating stars. At the end of the MS, the faster the stars initial rotation, the larger the convective core. This behaviour is valid at the three considered metallicities. We recall, however, the peculiar behaviour of the convective core of the 1.7 $M_\odot$ at different rotational velocities, owing to the conflicts between the pp-chains and CNO cycle (see above and Fig. 5, left panel).

At low metallicity, for the upper mass range of our sample (above ~7 $M_\odot$), and for the fastest rotational velocities ($\omega \gtrsim 0.8$), the merger of the core with the convective zone that develops above it modifies the behaviour at the end of the MS, refuelling it in fresh hydrogen and prolonging the MS duration (see Fig. 5, right panel). The core mass will have an effect on the final yields, as is discussed in Sect. 5.2.

4.4. Evolution of the surface velocity

Figure 6 shows the evolution of the surface velocities during the MS phase for the 1.7 and 15 $M_\odot$ stellar models. Close to the ZAMS, we see an abrupt decrease in v_{eq}. It corresponds to the time taken by the model to reach a quasi-equilibrium state (the initial flat Ω-profile is not at the equilibrium once the meridional circulation acts). We also see that the equatorial velocities are initially higher at lower metallicity for the models starting at the same ω. This is due to the larger compactness of the star at low Z: since the initial CNO content is lower, the star must compensate for this lack of catalyst elements during the core

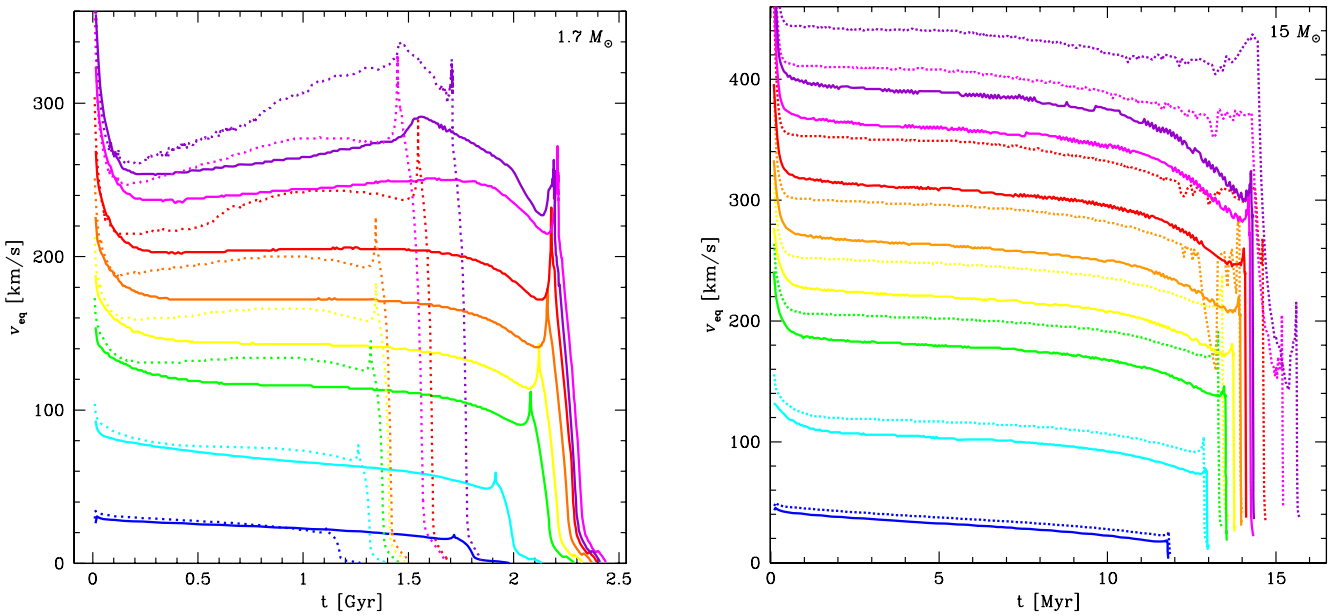

Fig. 6. Equatorial velocity evolution (same colour code as in Fig. 1) at $Z = 0.014$ (solid lines) and $Z = 0.002$ (dotted lines). *Left*: 1.7 $M_\odot$ models. *Right*: 15 $M_\odot$ models.

hydrogen-burning phase by adopting a more compact structure that allows a higher central temperature. With $v_{\rm eq,\,ini} = \Omega_{\rm ini} r$, and looking at Eq. (1), we find that for a given ω and a given mass, the initial equatorial velocity is $v_{\rm eq,\,ini} \sim r^{-\frac{5}{2}}$, and thus, is higher for a more compact star.

The surface angular velocity varies as a function of the time because of three main physical processes:

- the local conservation of the angular momentum, which modifies the angular velocity when the star contracts or expands;
- internal transport mechanisms (see Zahn 1992; Maeder & Zahn 1998), which redistribute the angular momentum throughout the star;
- stellar winds, which remove angular momentum from the stellar surface.

During the MS, our models develop an external meridional circulation cell (Gratton-Öpik cell, see e.g. Maeder 2009), which carries angular momentum from the inner part of the star to the surface, tending to accelerate it. The efficiency of the meridional circulation is greater for higher masses, for higher initial rotational rates and for higher metallicity. In contrast, the stellar mass loss due to radiative winds (Castor et al. 1975) tends to brake the stellar surface. As for the meridional circulation, the strength of the stellar winds is greater for higher mass stars, for higher rotational rates (Maeder & Meynet 2000), and for higher metallicities. There are thus two counteracting effects governing the evolution of the stellar surface velocity. For a given initial mass, rotation rate, and metallicity, their relative efficiency will govern the increase or decrease in the surface velocity during stellar life. We see from Fig. 6 that in the mass range studied here, the equatorial velocity remains roughly constant during the MS, however, according to Eq. (3), $v_{\rm crit}$ itself decreases during the MS, since $R_{\rm eq}$ is increasing. As a result, the ratio $v_{\rm eq}/v_{\rm crit}$ increases (see Ekström et al. 2008).

From Fig. 7, one sees that the contrast between the rotation rates of the core and of the envelope is stronger in slowly rotating stars than in faster rotating ones. This illustrates that the combined effects of meridional circulation and shears, which tend to flatten the Ω-profiles, are stronger in faster rotating stars. Similar qualitative behaviours are obtained for the whole mass and metallicity range considered here. The model with $\omega_{\rm ini} = 0.50$ (which is close to the peak of the rotation rate distribution according to Huang et al. 2010) shows a ratio $\Omega_{\rm cen}/\Omega_{\rm surf} \simeq 3$. At the moment, the ratio of $\Omega_{\rm cen}/\Omega_{\rm surf}$ has been estimated through asteroseismology in three slowly rotating B-type stars (Aerts 2008). The results range between 1 and 6. The present results overlap the observed range well, although the small amount of data does not allow a systematic and detailed comparison.

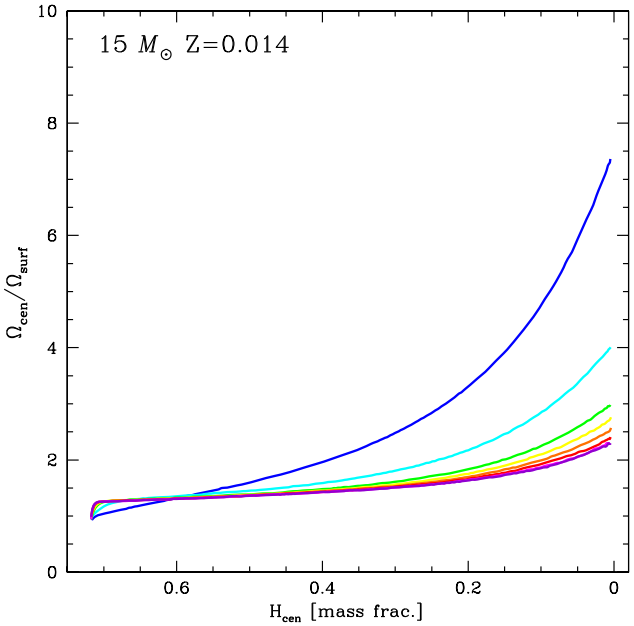

Fig. 7. $\Omega_{\rm centre}/\Omega_{\rm surface}$ ratio for the 15 $M_\odot$ models et $Z = 0.014$ (same colour code as in Fig. 1).

4.5. Surface abundances

The variations in the surface abundances at the end of the MS phase are shown in Fig. 8. We see, as already obtained in

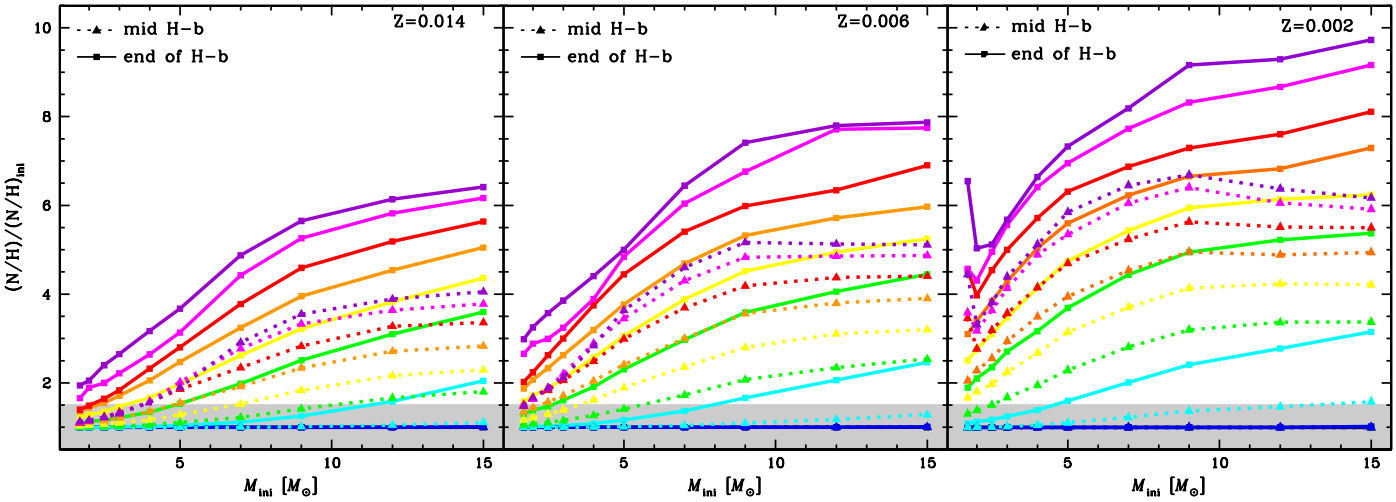

Fig. 8. N/H ratio at the end of the MS as a function of the initial mass for all the models. Models at $Z = 0.014$ (*left*), $Z = 0.006$ (*centre*), and $Z = 0.002$ (*right*).

previous works (Maeder & Meynet 2001), that for a given value of $\omega_{\rm ini}$[6], the enrichment is stronger at lower metallicities and for higher masses. This is true not only for the massive stars, but also for intermediate-mass stars.

In Fig. 8, the shadowed area corresponds to a variation of 0.2 dex with respect to the initial N/H ratio (corresponding roughly to the typical error bars in the measurements of abundances. For example, typical error bars in the VLT-FLAMES survey of massive stars for individual stars are estimated by the authors to be between 0.1 and 0.3 dex (Hunter et al. 2007). According to Nieva & Przybilla (2010), the typical error bars are systematically underestimated, and should rather be of the order of 0.3 dex. The models evolving out of this area will therefore have a strong enough enrichment to be observable. The dashed lines correspond to the mid-MS (when the central hydrogen mass fraction is half of its initial value), and the continuous lines to the end of the MS. At solar metallicity, the mixing is efficient enough in massive stars ($M \geq 9\,M_{\odot}$) to be observationally detectable, even for moderately rotating ($\omega \gtrsim 0.5$) stars, and already at the middle of the MS. For the lower masses, this is no longer true, and only stars with an initial mass above $4\,M_{\odot}$ are mixed enough to produce an observable enrichment at the middle of the MS, even for the fastest rotators. At the end of the MS, the enrichment is observable only for the most rapidly rotating stars for our $1.7\,M_{\odot}$ models ($\omega \gtrsim 0.8$).

At $Z = 0.002$, we see that the more efficient mixing makes the surface enrichment much more easily detectable, even for our lowest mass models. Indeed, all the stars with initial velocity $\omega_{\rm ini} > 0.60$ (yellow tracks) show sufficient enrichment at mid-MS, and $\omega_{\rm ini} > 0.50$ for the end of the MS.

5. Advanced phases

5.1. Blue loops

The physical mechanisms leading to the expansion or contraction of the envelope during the stellar life are still poorly understood, and are being debated (Renzini et al. 1992; Stancliffe et al. 2009). According to Lauterborn et al. (1971), the occurrence of a blue loop during core He-burning depends on the relation between the gravitational potential of the core and a critical potential that is mass dependent, as well as on the internal hydrogen profile. Any process able to modify either the total mass, the mass or radius of the core, or the hydrogen abundance profile will affect the occurrence of a blue loop.

Rotation affects all these quantities in various ways, depending on the rotation rate, as can be seen in Fig. 9. Metallicity also plays a role, since rotational mixing occurs differently at different metallicities. A general feature is that rotation increases the time spent on the loop. An exception to that are the models at $Z_{\odot}$ rotating with $\omega_{\rm ini} = 0.8$ and 0.9, where the loop is suppressed.

At non-solar metallicity, the difference in luminosity between the leftwards excursion at the start of the loop and the redwards return movement is widened by rotation. The widening occurs toward both lower starting luminosity and higher final luminosity. In the most extreme cases, the lowering of the starting luminosity might reach the luminosity of the crossing of the Hertzsprung gap. In that case, the model "jumps" directly onto the top of the loop, avoiding the first RSG phase. For those models, most of the core He-burning occurs thus in the blue part of the HRD ($\log(T_{\rm eff}\ [{\rm K}]) \gtrsim 4.0$). Such behaviour will reduce the number of RSG at low metallicity.

We will dedicate a future paper to more detailed study of the implication of this effect on the Cepheid population predicted by our models.

5.2. Mass ejections of various elements

In Table 1, we present the ejected masses for H, He, C, N, O, and remaining metals, as well as the CO-core mass and the remnant mass (computed as in Hirschi et al. 2005, and Georgy et al. 2009). We see that rotation increases the mass of the CO core significantly, and this in a larger way at lower metallicity, which matches the result of a higher mixing in lower Z. For the SMC, the increase amounts to 43%, while for the LMC and Galaxy it is 27% and 25%, respectively, for the models with $\omega_{\rm ini} = 0.95$. This table is qualitatively representative of the trends obtained for the higher part of our mass range. We do not discuss here the ejected masses for the models of our sample that become AGB stars, since we have not followed these models through this phase.

[6] We focus our discussion on comparing models with the same $\omega_{\rm ini}$. The trends can differ slightly if we considered for example the same $v_{\rm eq,\,ini}$. The detailed trends can be obtained by the mean of the tables provided in this paper, or directly from the available electronic data.

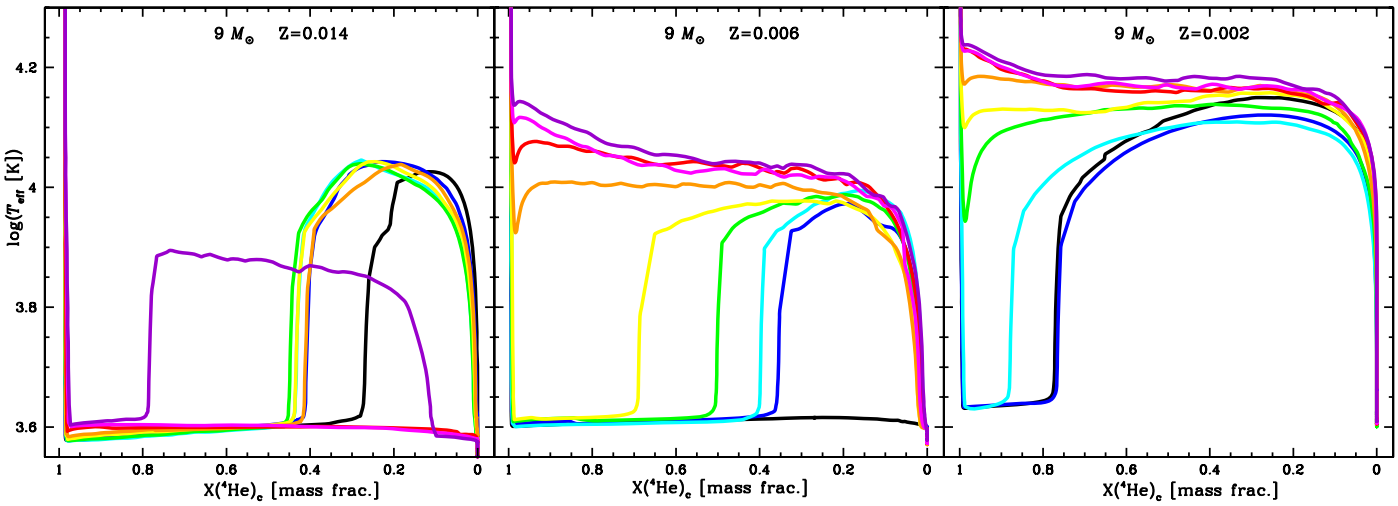

Fig. 9. $T_{\rm eff}$ as a function of the helium mass fraction in the core. Models at $Z = 0.014$ (*left*), $Z = 0.006$ (*centre*), and $Z = 0.002$ (*right*).

Table 1. CO-core mass, remnant mass, and ejected masses in hydrogen, helium, carbon, nitrogen, oxygen, and remaining heavy elements for the 15 $M_{\odot}$ models at the three metallicities and all the rotation rates.

	$\omega_{\rm ini}$	$M_{\rm CO}$	$M_{\rm rem}$ [1]	$M_{\rm H}^{\rm ej}$	$M_{\rm He}^{\rm ej}$	$M_{\rm C}^{\rm ej}$	$M_{\rm N}^{\rm ej}$	$M_{\rm O}^{\rm ej}$	$M_{\rm other\ heavies}^{\rm ej}$
$Z = 0.002$	0.00	2.6961	1.4265	6.8329	5.0423	0.3638	0.0056	0.6237	0.2129
	0.10	3.0113	1.4915	6.5290	4.8647	0.3795	0.0058	0.9746	0.1920
	0.30	3.1037	1.5097	6.0193	5.1801	0.4782	0.0066	1.1124	0.1496
	0.50	3.0275	1.4947	5.5969	5.2227	0.5249	0.0071	1.1904	0.1022
	0.60	2.8358	1.4556	5.8074	5.5233	0.5636	0.0084	1.0755	0.0744
	0.70	3.3706	1.5619	5.1903	4.8331	0.5772	0.0071	1.5936	0.1491
	0.80	3.3276	1.5535	4.9495	5.2080	0.6117	0.0079	1.5929	0.1397
	0.90	3.7427	1.6335	4.3507	4.8306	0.6983	0.0069	1.9760	0.0207
	0.95	3.8653	1.6568	4.1340	4.7515	0.7848	0.0069	2.0926	0.0442
$Z = 0.006$	0.00	2.6607	1.4191	6.2795	4.8178	0.4218	0.0167	0.6678	0.1142
	0.10	2.8571	1.4600	5.7171	4.5974	0.3637	0.0162	0.8697	0.2075
	0.30	3.1193	1.5128	5.2323	4.7427	0.4892	0.0167	1.1535	0.1483
	0.50	3.0771	1.5045	5.2111	5.0265	0.5610	0.0185	1.1342	0.1446
	0.60	2.9607	1.4815	5.1949	5.0690	0.5576	0.0192	1.1200	0.1409
	0.70	3.1077	1.5105	5.2193	4.7928	0.6010	0.0203	1.4027	0.1191
	0.80	3.1568	1.5202	4.9762	4.7993	0.5864	0.0204	1.5126	0.1071
	0.90	3.4196	1.5714	3.9929	4.4800	0.6119	0.0180	1.6830	0.1459
	0.95	3.4000	1.5676	3.8333	4.3666	0.6419	0.0175	1.6814	0.1237
$Z = 0.014$	0.00	2.4065	1.3655	5.8070	4.8193	0.2956	0.0400	0.4983	0.2577
	0.10	2.7714	1.4422	4.8298	4.2007	0.3913	0.0337	0.8906	0.1801
	0.30	3.3153	1.5511	3.4444	3.5356	0.5674	0.0272	1.4047	0.1666
	0.50	3.1867	1.5260	3.4473	3.7215	0.6409	0.0287	1.3235	0.1908
	0.60	3.2256	1.5337	3.4455	3.8259	0.5787	0.0309	1.4612	0.1081
	0.70	3.2558	1.5395	3.4518	3.9198	0.5009	0.0334	1.5509	0.0936
	0.80	2.9022	1.4694	4.1405	4.7817	0.5307	0.0392	1.0723	0.1649
	0.90	2.9977	1.4888	4.0481	4.3689	0.6091	0.0382	1.2925	0.1168
	0.95	3.0261	1.4944	4.2465	4.6714	0.5045	0.0420	1.1951	0.1783

Notes. All masses are expressed in $M_{\odot}$ units. [(1)] The remnant mass is computed following the same method as in Hirschi et al. (2005) and Georgy et al. (2009).

The general trends concerning the ejected elements in rotating models are the following.

- Hydrogen is mostly depleted (~60% in the SMC and LMC models, and 73% in the Galactic models); this reflects the fact that more mass is processed by nuclear burning in rotating stars.
- Carbon and oxygen tend to be produced more. Comparing the models with $\omega_{\rm ini} = 0$ and $\omega_{\rm ini} = 0.95$, the increase in the ejected mass of carbon amounts to a factor of 2.15 for the SMC models, 1.52 for the LMC, and 1.71 for the Galactic models. The increase in the ejected mass of oxygen amounts to a factor of 3.36 for the SMC, 2.52 for the LMC, and 2.40 for the Galaxy. In the Galactic case, the higher increase in C and O occurs for models with $\omega_{\rm ini} = 0.50$ and 0.60, respectively, with a maximal increase by a factor of 2.06 and 3.11, respectively.

Helium, nitrogen and the remaining metals do not show any definite trend. One also notes that even at high rotation, we do not observe any production of primary nitrogen, in these models.

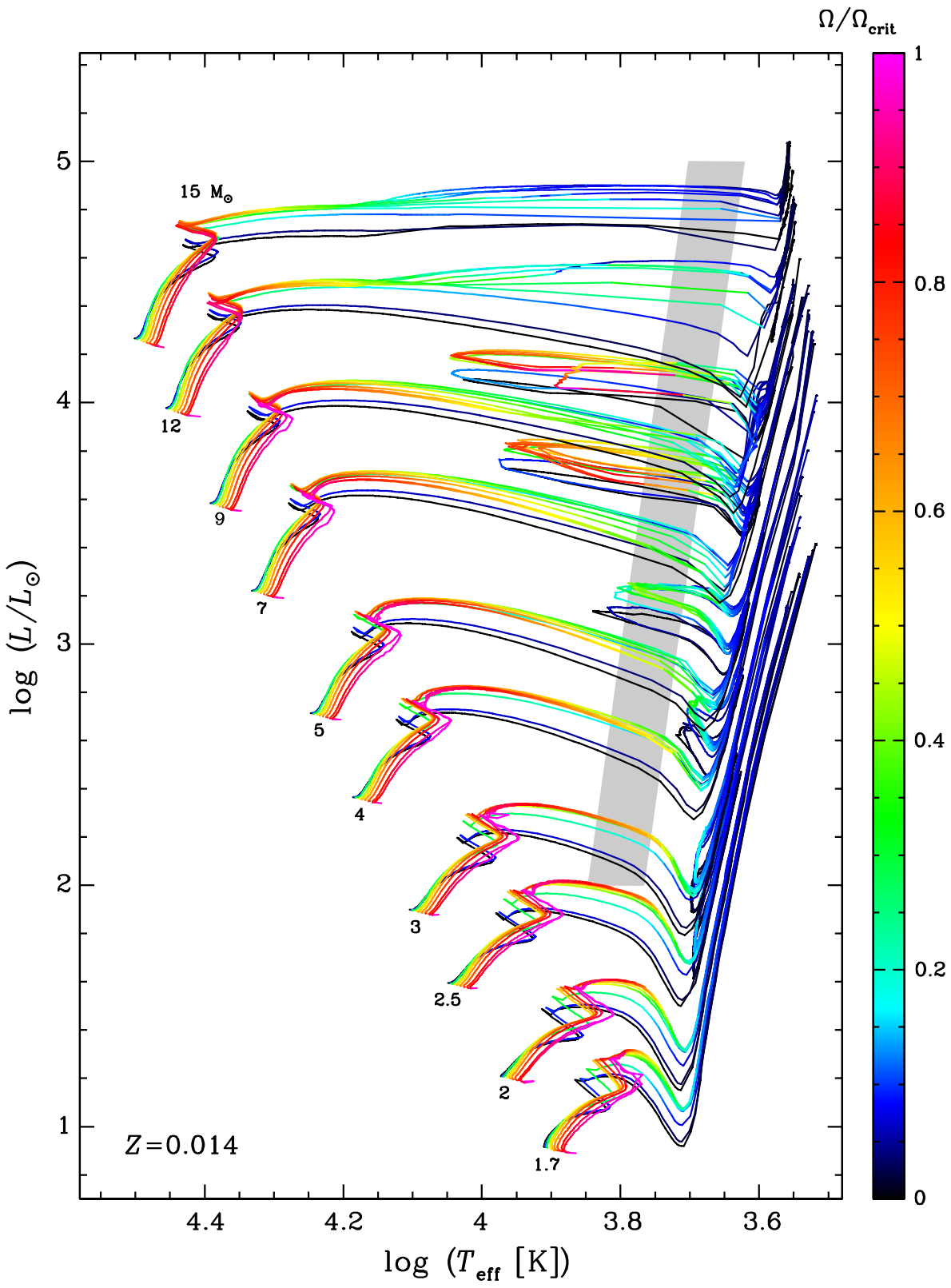

Fig. 10. HRD for $Z = 0.014$. The colour code represents the ratio Ω/Ω_{crit} (scale on the *right*). For each mass, the order of the curves on the ZAMS (bottom-left point of the curves) goes from the lowest to the highest initial rotation velocity from left to right.

6. Conclusions

In this paper, we have presented an extended database of rotating stellar models at three different metallicities, for nine different initial rotation parameters and ten different masses, in the line of the previous large grid of stellar models (Ekström et al. 2012). The computations account for an accurate follow-up of the angular-momentum content, and for the stellar-wind anisotropy. Moreover, they allow an estimate of the amount of mass that the star should lose mechanically in an equatorial disc

when rotating at the critical velocity. This database will be particularly useful for constructing synthetic populations of stars, accounting for mass, rotation, and metallicity distributions.

In this first paper, we presented some general results on the behaviour of the models in the HRD, their lifetime, surface velocities, chemical enrichment, and advanced phases behaviour. In the second paper of this series (Granada et al. 2013), extensive comparison between the results presented here and observation concerning Be stars were done, particularly concerning the mean mass-loss rates during the critical-rotation phase, disc mass, and lifetimes.

Acknowledgements. The authors thank the anonymous referee, whose useful comments helped to improve this work. C.G. acknowledges support from EU-FP7-ERC-2012-St Grant 306901.

References

Aerts, C. 2008, in Massive Stars as cosmic Engines, eds. F. Bresolin, P. A. Crowther, & J. Puls (Cambridge: CUP), IAU Symp., 250, 237
Carciofi, A. C., Domiciano de Souza, A., Magalhães, A. M., Bjorkman, J. E., & Vakili, F. 2008, ApJ, 676, L41
Castor, J. I., Abbott, D. C., & Klein, R. I. 1975, ApJ, 195, 157
Chaboyer, B., & Zahn, J. 1992, A&A, 253, 173
Cyburt, R. H., Fields, B. D., & Olive, K. A. 2003, Phys. Lett. B, 567, 227
Ekström, S., Meynet, G., Maeder, A., & Barblan, F. 2008, A&A, 478, 467
Ekström, S., Georgy, C., Eggenberger, P., et al. 2012, A&A, 537, A146
Georgy, C. 2010, Ph.D. Thesis, Geneva Observatory, Geneva University
Georgy, C., Meynet, G., Walder, R., Folini, D., & Maeder, A. 2009, A&A, 502, 611
Georgy, C., Meynet, G., & Maeder, A. 2011, A&A, 527, A52
Granada, A., Ekström, S., Georgy, C., et al. 2013, A&A, 553, A25 (Paper II)
Hirschi, R., Meynet, G., & Maeder, A. 2005, A&A, 443, 581
Huang, W., & Gies, D. R. 2006, ApJ, 648, 580
Huang, W., Gies, D. R., & McSwain, M. V. 2010, ApJ, 722, 605
Hunter, I., Dufton, P. L., Smartt, S. J., et al. 2007, A&A, 466, 277
Lauterborn, D., Refsdal, S., & Weigert, A. 1971, A&A, 10, 97
Maeder, A. 1997, A&A, 321, 134
Maeder, A. 2002, A&A, 392, 575
Maeder, A. 2003, A&A, 399, 263
Maeder, A. 2009, Physics, Formation and Evolution of Rotating Stars (Springer)
Maeder, A., & Meynet, G. 2000, A&A, 361, 159
Maeder, A., & Meynet, G. 2001, A&A, 373, 555
Maeder, A., & Zahn, J.-P. 1998, A&A, 334, 1000
Martayan, C., Frémat, Y., Hubert, A.-M., et al. 2007, A&A, 462, 683
Martayan, C., Baade, D., & Fabregat, J. 2010, A&A, 509, A11
Mathis, S., Palacios, A., & Zahn, J.-P. 2004, A&A, 425, 243
Meynet, G., & Maeder, A. 2000, A&A, 361, 101
Mowlavi, N., Eggenberger, P., Meynet, G., et al. 2012, A&A, 541, A41
Neiner, C., Mathis, S., Saio, H., et al. 2012, A&A, 539, A90
Nieva, M.-F., & Przybilla, N. 2010, in Hot and Cool: Bridging Gaps in Massive Star Evolution, eds. C. Leitherer, P. D. Bennett, P. W. Morris, & J. T. Van Loon, ASP Conf. Ser., 425, 146
Renzini, A., Greggio, L., Ritossa, C., & Ferrario, L. 1992, ApJ, 400, 280
Stancliffe, R. J., Chieffi, A., Lattanzio, J. C., & Church, R. P. 2009, PASA, 26, 203
Talon, S., & Zahn, J.-P. 1997, A&A, 317, 749
Tammann, G. A., Sandage, A., & Reindl, B. 2003, A&A, 404, 423
Vinicius, M. M. F., Zorec, J., Leister, N. V., & Levenhagen, R. S. 2006, A&A, 446, 643
Zahn, J.-P. 1992, A&A, 265, 115
Zorec, J., Frémat, Y., Domiciano de Souza, A., et al. 2011, A&A, 526, A87

Pages 13 to 17 are available in the electronic edition of the journal at http://www.aanda.org

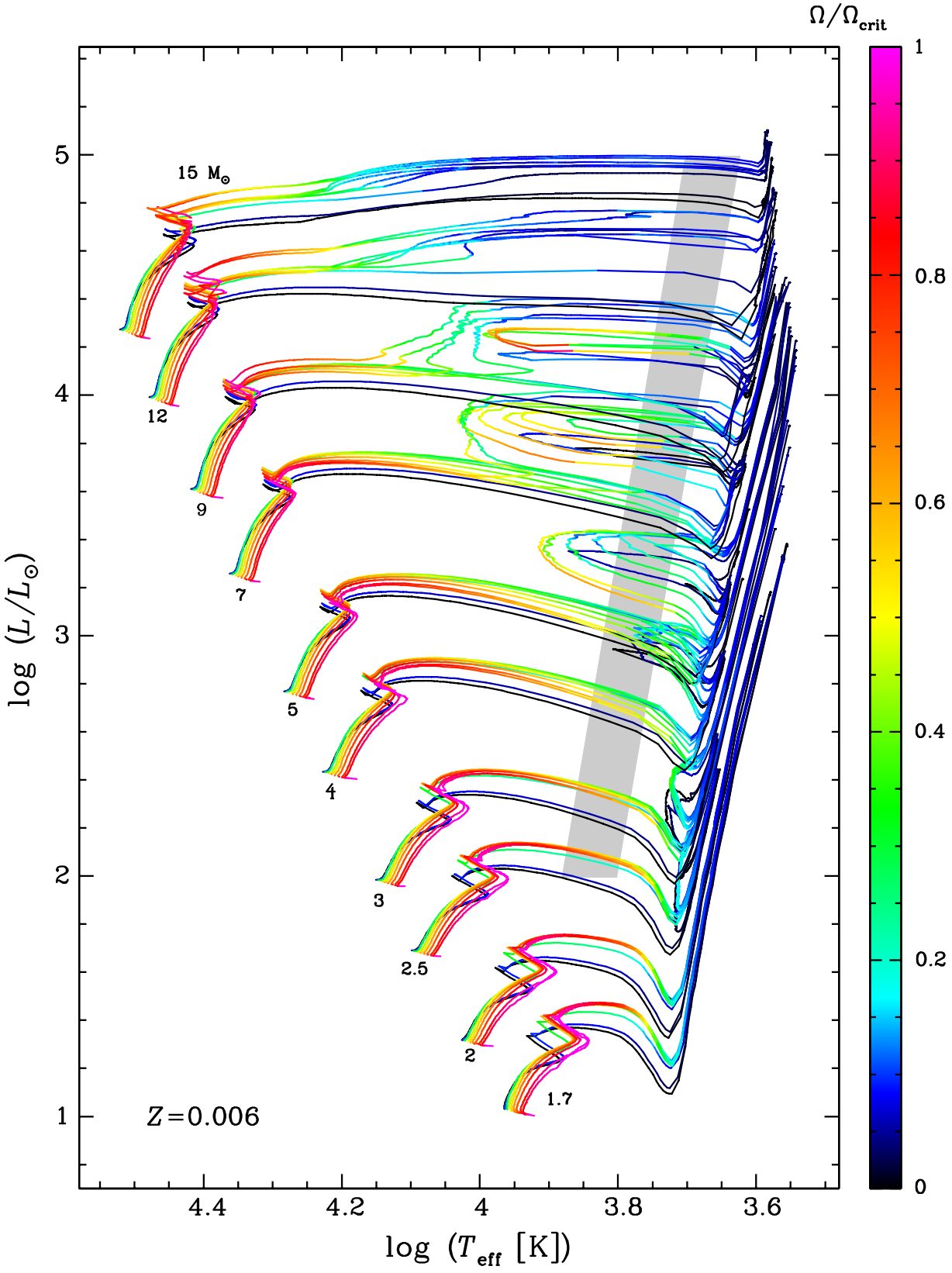

Fig. 11. Same as Fig. 10, but for $Z = 0.006$.

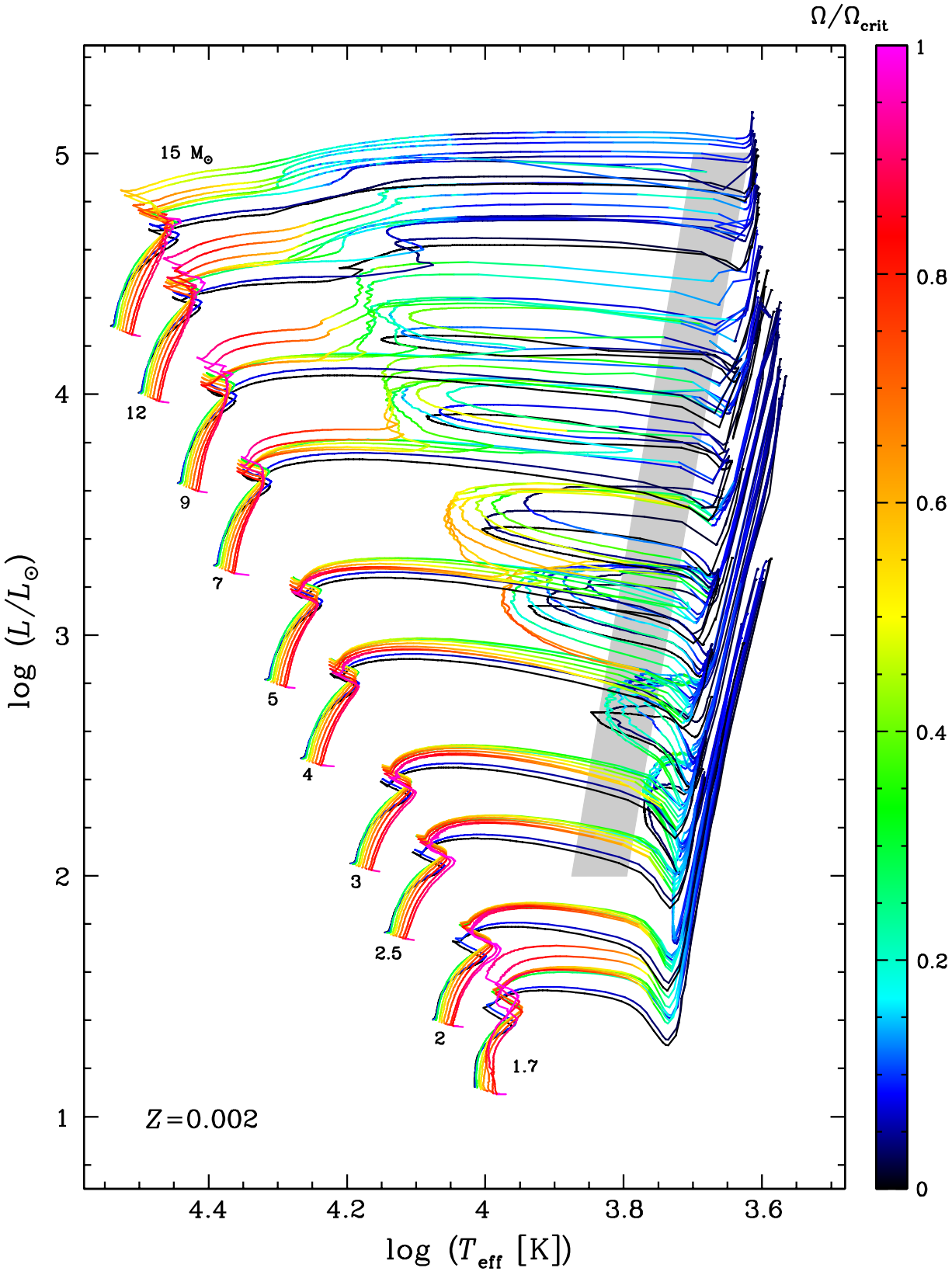

Fig. 12. Same as Fig. 10, but for $Z = 0.002$.

Table 2. Main parameters of A-B stars at $Z = 0.014 = Z_\odot$.

				End of H-burning							End of He-burning							End of C-burning						
$M_{\rm ini}$	$\Omega/\Omega_{\rm crit,\,ini}$	$v_{\rm eq}$	$\bar{v}_{\rm MS}$	$\tau_{\rm H}$	M	$v_{\rm eq}$	$v_{\rm eq}/v_{\rm crit}$	$Y_{\rm surf}$	N/C	N/O	$\tau_{\rm He}$	M	$P_{\rm rot}$	$\Omega_{\rm c}/\Omega_{\rm s}$	$Y_{\rm surf}$	N/C	N/O	$\tau_{\rm C}$	M	$P_{\rm rot}$	$\Omega_{\rm c}/\Omega_{\rm s}$	$Y_{\rm surf}$	N/C	N/O
$M_\odot$		km s^{-1}		Myr	$M_\odot$	km s^{-1}			mass fract.		Myr	$M_\odot$	day			mass fract.		kyr	$M_\odot$	day			mass fract.	
15.00	0.00	0.	0.	11.015	14.81	0.	0.000	0.2660	0.2885	0.1152	1.315	13.34	–	–	0.3054	2.0811	0.5211	4.721	13.25	–	–	0.3390	3.0660	0.7360
15.00	0.10	44.	31.	11.661	14.79	19.	0.043	0.2660	0.2931	0.1166	1.528	12.23	$2.833\cdot10^6$	$2.579\cdot10^7$	0.3235	2.3726	0.6413	2.868	12.14	$3.780\cdot10^6$	$3.192\cdot10^9$	0.3480	3.0057	0.7913
15.00	0.30	132.	99.	12.842	14.73	76.	0.182	0.2704	0.7316	0.2442	1.404	11.01	$1.424\cdot10^6$	$2.842\cdot10^7$	0.3564	3.7688	0.8513	1.516	10.89	$1.429\cdot10^6$	$2.535\cdot10^9$	0.3769	4.3558	0.9605
15.00	0.50	241.	173.	13.399	14.71	139.	0.329	0.2835	1.7907	0.4568	1.365	11.19	$7.856\cdot10^5$	$2.153\cdot10^7$	0.3719	5.5490	0.9928	2.121	11.07	$1.106\cdot10^6$	$2.685\cdot10^9$	0.3954	6.5423	1.1182
15.00	0.60	277.	213.	13.633	14.69	174.	0.409	0.2922	2.6259	0.5704	1.408	11.28	$4.914\cdot10^5$	$1.583\cdot10^7$	0.3964	7.6476	1.1547	1.540	11.17	$7.067\cdot10^5$	$1.974\cdot10^9$	0.4161	8.8192	1.2717
15.00	0.70	333.	254.	13.836	14.68	206.	0.480	0.3008	3.7090	0.6758	1.452	11.41	$2.126\cdot10^5$	$7.387\cdot10^6$	0.4100	10.2467	1.2709	1.216	11.29	$3.946\cdot10^5$	$1.142\cdot10^9$	0.4264	11.7377	1.3780
15.00	0.80	396.	299.	13.983	14.68	240.	0.550	0.3087	5.0934	0.7694	1.318	12.48	$7.165\cdot10^4$	$2.802\cdot10^6$	0.4022	11.9872	1.2671	2.687	12.36	$1.263\cdot10^5$	$4.776\cdot10^8$	0.4207	13.9606	1.3818
15.00	0.90	501.	348.	14.123	14.67	272.	0.614	0.3164	6.9790	0.8560	1.418	12.26	$9.525\cdot10^4$	$4.267\cdot10^6$	0.3976	14.7608	1.2829	2.479	12.13	$1.445\cdot10^5$	$6.067\cdot10^8$	0.4180	16.9923	1.4089
15.00	0.95	525.	375.	14.189	14.66	287.	0.639	0.3199	8.1555	0.8963	1.441	12.63	$5.908\cdot10^4$	$2.815\cdot10^6$	0.4024	17.4288	1.3403	2.543	12.51	$9.546\cdot10^4$	$4.241\cdot10^8$	0.4208	20.0816	1.4607
12.00	0.00	0.	0.	15.331	11.94	0.	0.000	0.2660	0.2885	0.1152	2.124	11.36	–	–	0.3007	1.8374	0.4918	7.858	11.31	–	–	0.3072	1.9788	0.5280
12.00	0.10	41.	31.	16.182	11.93	23.	0.054	0.2660	0.2886	0.1152	2.150	11.21	$1.665\cdot10^5$	$1.833\cdot10^6$	0.3053	2.3165	0.5937	6.859	11.15	$4.957\cdot10^5$	$6.823\cdot10^8$	0.3082	2.4007	0.6104
12.00	0.30	138.	98.	17.862	11.91	88.	0.216	0.2674	0.5172	0.1846	1.812	10.65	$1.205\cdot10^5$	$2.808\cdot10^6$	0.3193	3.0294	0.6752	6.705	10.57	$2.214\cdot10^5$	$6.239\cdot10^8$	0.3287	3.2817	0.7213
12.00	0.50	215.	171.	18.540	11.91	164.	0.397	0.2755	1.4363	0.3818	1.892	10.40	$8.402\cdot10^4$	$2.809\cdot10^6$	0.3272	4.4674	0.7804	6.134	10.31	$1.327\cdot10^5$	$5.280\cdot10^8$	0.3502	5.3748	0.8895
12.00	0.60	284.	210.	18.762	11.90	206.	0.493	0.2813	2.1637	0.4829	2.125	10.30	$7.799\cdot10^4$	$3.027\cdot10^6$	0.3362	5.8284	0.8577	3.803	10.22	$1.292\cdot10^5$	$5.572\cdot10^8$	0.3611	6.9967	0.9729
12.00	0.70	333.	252.	18.902	11.90	252.	0.594	0.2879	3.2498	0.5875	2.006	10.84	$3.031\cdot10^4$	$1.370\cdot10^6$	0.3518	8.1420	0.9623	6.097	10.76	$5.262\cdot10^4$	$3.531\cdot10^8$	0.3722	9.6176	1.0656
12.00	0.80	404.	298.	19.000	11.91	302.	0.701	0.2944	4.7996	0.6845	2.178	10.71	$3.647\cdot10^4$	$1.882\cdot10^6$	0.3428	10.5711	0.9748	0.063	10.64	$5.642\cdot10^4$	$5.408\cdot10^7$	0.3712	12.7958	1.1021
12.00	0.90	477.	349.	19.126	11.90	331.	0.749	0.3026	7.3874	0.7816	2.400	10.76	$3.236\cdot10^4$	$1.809\cdot10^6$	0.3508	15.2610	1.0404	0.072	10.69	$5.110\cdot10^4$	$5.208\cdot10^7$	0.3746	17.8632	1.1482
12.00	0.95	556.	375.	19.302	11.89	333.	0.748	0.3071	9.0862	0.8352	2.357	10.80	$3.044\cdot10^4$	$1.837\cdot10^6$	0.3552	18.2425	1.0840	0.066	10.73	$4.571\cdot10^4$	$5.457\cdot10^7$	0.3780	21.0351	1.1874
9.00	0.00	0.	0.	26.262	8.99	0.	0.000	0.2660	0.2885	0.1152	3.492	8.80	–	–	0.2824	1.6090	0.4219							
9.00	0.10	40.	31.	27.541	8.99	24.	0.060	0.2660	0.2885	0.1152	3.502	8.81	$2.852\cdot10^4$	$3.537\cdot10^5$	0.2924	2.0461	0.5234							
9.00	0.30	130.	94.	30.354	8.99	91.	0.230	0.2664	0.3841	0.1454	3.296	8.77	$1.501\cdot10^4$	$4.052\cdot10^5$	0.3169	3.0518	0.6696	0.041	8.73	$5.781\cdot10^4$	$7.649\cdot10^7$	0.3172	3.2003	0.6840
9.00	0.50	216.	163.	31.464	8.99	170.	0.427	0.2709	1.0243	0.3023	3.351	8.76	$1.001\cdot10^4$	$3.890\cdot10^5$	0.3285	4.7700	0.7896	0.009	8.72	$3.673\cdot10^4$	$7.449\cdot10^7$	0.3290	4.9811	0.8029
9.00	0.60	261.	200.	31.685	8.99	213.	0.527	0.2748	1.5832	0.3960	3.450	8.78	$8.019\cdot10^3$	$3.767\cdot10^5$	0.3330	6.1149	0.8446							
9.00	0.70	311.	240.	31.918	8.99	259.	0.632	0.2799	2.4400	0.4972	3.610	8.78	$6.505\cdot10^3$	$3.524\cdot10^5$	0.3357	8.1696	0.8956							
9.00	0.80	381.	284.	31.971	8.99	316.	0.758	0.2847	3.6168	0.5868	4.446	8.65	$6.841\cdot10^3$	$4.341\cdot10^5$	0.3334	10.8419	0.9206							
9.00	0.90	466.	335.	32.264	8.99	377.	0.887	0.2913	5.4922	0.6907	4.356	8.66	$6.055\cdot10^3$	$4.398\cdot10^5$	0.3285	13.7674	0.9446							
9.00	0.95	492.	364.	32.482	8.98	380.	0.888	0.2962	7.0486	0.7520	4.610	8.73	$9.626\cdot10^3$	$7.050\cdot10^5$	0.3296	15.9175	0.9689							
7.00	0.00	0.	0.	41.722	7.00	0.	0.000	0.2660	0.2885	0.1152	6.919	6.92	–	–	0.2792	1.5177	0.3964							
7.00	0.10	40.	30.	44.651	7.00	23.	0.060	0.2660	0.2885	0.1152	7.138	6.92	$1.679\cdot10^4$	$2.398\cdot10^5$	0.2880	1.8383	0.4734							
7.00	0.30	124.	89.	49.304	7.00	86.	0.226	0.2661	0.3302	0.1285	6.663	6.90	$6.959\cdot10^3$	$2.238\cdot10^5$	0.3104	2.7399	0.6210							
7.00	0.50	207.	154.	51.151	7.00	160.	0.420	0.2685	0.7166	0.2341	6.795	6.89	$4.772\cdot10^3$	$2.193\cdot10^5$	0.3190	4.0102	0.7192							
7.00	0.60	253.	190.	51.688	7.00	203.	0.527	0.2711	1.1053	0.3149	7.174	6.88	$4.221\cdot10^3$	$2.268\cdot10^5$	0.3221	4.9466	0.7671							
7.00	0.70	301.	227.	51.999	7.00	250.	0.641	0.2743	1.6250	0.3975	6.990	6.89	$3.169\cdot10^3$	$2.037\cdot10^5$	0.3248	6.3624	0.8174							
7.00	0.80	352.	269.	52.238	7.00	312.	0.788	0.2774	2.2416	0.4701	7.431	6.90	$2.645\cdot10^3$	$1.956\cdot10^5$	0.3266	8.3759	0.8637							
7.00	0.90	433.	320.	52.466	7.00	364.	0.905	0.2826	3.3200	0.5621	8.239	6.90	$2.440\cdot10^3$	$2.059\cdot10^5$	0.3285	11.3917	0.9088							
7.00	0.95	477.	348.	52.900	6.99	362.	0.892	0.2871	4.3773	0.6282	8.465	6.89	$2.508\cdot10^3$	$2.187\cdot10^5$	0.3291	13.0544	0.9246							
5.00	0.00	0.	0.	88.195	5.00	0.	0.000	0.2660	0.2885	0.1152	19.380	4.96	–	–	0.2792	1.4819	0.3864							
5.00	0.10	34.	28.	94.322	5.00	21.	0.060	0.2660	0.2885	0.1152	18.712	4.96	$8.100\cdot10^3$	$1.415\cdot10^5$	0.2859	1.6282	0.4269							
5.00	0.30	116.	83.	104.456	5.00	76.	0.218	0.2660	0.3026	0.1197	17.918	4.95	$2.531\cdot10^3$	$9.568\cdot10^4$	0.3071	2.4483	0.5752							
5.00	0.50	192.	143.	109.085	5.00	143.	0.409	0.2670	0.4995	0.1781	16.800	4.95	$1.416\cdot10^3$	$7.935\cdot10^4$	0.3154	3.3394	0.6627							
5.00	0.60	234.	176.	110.343	5.00	181.	0.516	0.2684	0.7165	0.2329	17.669	4.95	$1.252\cdot10^3$	$8.018\cdot10^4$	0.3190	4.0502	0.7107							
5.00	0.70	277.	211.	111.232	5.00	224.	0.629	0.2703	1.0124	0.2950	17.447	4.95	$1.049\cdot10^3$	$7.912\cdot10^4$	0.3205	4.8353	0.7467							
5.00	0.80	342.	251.	112.264	5.00	282.	0.783	0.2715	1.2602	0.3371	18.920	4.95	$9.469\cdot10^2$	$8.049\cdot10^4$	0.3225	5.8563	0.7836							
5.00	0.90	404.	298.	112.853	5.00	328.	0.904	0.2733	1.5533	0.3806	20.244	4.95	$8.089\cdot10^2$	$7.853\cdot10^4$	0.3232	7.1672	0.8163							
5.00	0.95	462.	326.	113.858	4.99	316.	0.866	0.2771	2.1374	0.4527	21.160	4.94	$8.364\cdot10^2$	$8.189\cdot10^4$	0.3256	8.1090	0.8382							
4.00	0.00	0.	0.	152.088	4.00	0.	0.000	0.2660	0.2885	0.1152	37.750	3.97	–	–	0.2823	1.5023	0.3912							
4.00	0.10	32.	26.	160.880	4.00	20.	0.058	0.2660	0.2885	0.1152	42.425	3.97	$2.471\cdot10^3$	$4.529\cdot10^4$	0.2873	1.5716	0.4126							
4.00	0.30	98.	78.	178.575	4.00	68.	0.210	0.2660	0.2951	0.1172	35.069	3.97	$9.885\cdot10^2$	$4.472\cdot10^4$	0.3077	2.2908	0.5518							
4.00	0.50	169.	136.	187.477	4.00	129.	0.399	0.2666	0.4202	0.1554	34.852	3.97	$8.134\cdot10^2$	$5.097\cdot10^4$	0.3167	3.0686	0.6380							
4.00	0.60	206.	167.	190.190	4.00	164.	0.506	0.2674	0.5617	0.1941	33.704	3.97	$5.941\cdot10^2$	$4.237\cdot10^4$	0.3187	3.5117	0.6695							
4.00	0.70	248.	201.	192.706	4.00	203.	0.627	0.2687	0.7616	0.2421	33.980	3.97	$4.964\cdot10^2$	$4.076\cdot10^4$	0.3213	4.1455	0.7103							
4.00	0.80	295.	239.	194.065	4.00	260.	0.795	0.2696	0.9224	0.2750	35.455	3.97	$4.324\cdot10^2$	$4.007\cdot10^4$	0.3227	4.9073	0.7418							
4.00	0.90	392.	284.	195.595	4.00	282.	0.849	0.2712	1.1427	0.3159	37.172	3.97	$3.897\cdot10^2$	$4.132\cdot10^4$	0.3245	5.7566	0.7737							
4.00	0.95	423.	312.	198.351	3.99	282.	0.849	0.2743	1.5901	0.3846	37.370	3.96	$3.954\cdot10^2$	$4.232\cdot10^4$	0.3276	6.4637	0.7997							
3.00	0.00	0.	0.	320.600	3.00	0.	0.000	0.2660	0.2885	0.1152	117.109	2.99	–	–	0.2868	1.5318	0.3928							
3.00	0.10	30.	25.	338.503	3.00	18.	0.057	0.2660	0.2885	0.1152	125.295	2.99	$9.850\cdot10^2$	$2.258\cdot10^4$	0.2906	1.5399	0.3994							
3.00	0.30	92.	73.	378.862	3.00	61.	0.205	0.2660	0.2913	0.1161	111.205	2.98	$4.318\cdot10^2$	$2.201\cdot10^4$	0.3106	2.1840	0.5285							
3.00	0.50	158.	127.	400.944	3.00	116.	0.395	0.2664	0.3698	0.1402	97.083	2.98	$2.641\cdot10^2$	$2.010\cdot10^4$	0.3213	2.8644	0.6132							
3.00	0.60	214.	156.	408.242	3.00	146.	0.497	0.2670	0.4725	0.1697	98.701	2.98	$2.552\cdot10^2$	$2.032\cdot10^4$	0.3244	3.3040	0.6518							
3.00	0.70	233.	188.	413.122	3.00	181.	0.614	0.2677	0.5880	0.1993	101.601	2.98	$2.129\cdot10^2$	$1.991\cdot10^4$	0.3261	3.7223	0.6762							
3.00	0.80	276.	224.	417.548	3.00	234.	0.788	0.2680	0.6515	0.2140	102.865	2.98	$1.970\cdot10^2$	$2.061\cdot10^4$	0.3281	4.3228	0.7081							
3.00	0.90	367.	267.	420.785	3.00	289.	0.997	0.2697	0.8674	0.2608	109.725	2.98	$1.803\cdot10^2$	$2.026\cdot10^4$	0.3278	4.8606	0.7256							
3.00	0.95	411.	293.	422.412	3.00	225.	0.748	0.2719	1.1641	0.3145	105.941	2.98	$1.928\cdot10^2$	$2.302\cdot10^4$	0.3314	5.3924	0.7517							
2.50	0.00	0.	0.	537.964	2.50	0.	0.000	0.2660	0.2885	0.1152	236.764	2.49	–	–	0.2852	1.4444	0.3662							
2.50	0.10	29.	24.	555.638	2.50	17.	0.058	0.2660	0.2885	0.1152	253.558	2.49	$9.509\cdot10^2$	$1.998\cdot10^4$	0.2884	1.4097	0.3648							
2.50	0.30	99.	70.	622.923	2.50	57.	0.200	0.2660	0.2900	0.1156	205.343	2.49	$3.458\cdot10^2$	$1.884\cdot10^4$	0.3080	2.0094	0.4834							
2.50	0.50	151.	121.	665.370	2.50	109.	0.389	0.2663	0.3491	0.1338	185.800	2.49	$2.206\cdot10^2$	$1.648\cdot10^4$	0.3206	2.6893	0.5737							
2.50	0.60	185.	150.	677.421	2.50	139.	0.496	0.2668	0.4262	0.1559	191.139	2.48	$2.044\cdot10^2$	$1.748\cdot10^4$	0.3230	3.0078	0.5997							
2.50	0.70	223.	180.	687.051	2.50	173.	0.616	0.2674	0.5150	0.1795	182.884	2.49	$1.598\cdot10^2$	$1.532\cdot10^4$	0.3249	3.3772	0.6262							
2.50	0.80	291.	215.	695.645	2.50	222.	0.784	0.2676	0.5592	0.1903	193.384	2.48	$1.577\cdot10^2$	$1.729\cdot10^4$	0.3271	3.8853	0.6559							
2.50	0.90	316.	257.	702.516	2.50	235.	0.827	0.2691	0.7478	0.2333	193.248	2.48	$1.471\cdot10^2$	$1.787\cdot10^4$	0.3299	4.5669	0.6898							
2.50	0.95	392.	281.	704.202	2.50	228.	0.800	0.2711	1.0004	0.2816	194.550	2.48	$1.478\cdot10^2$	$1.814\cdot10^4$	0.3301	4.7606	0.6958							
2.00	0.00	0.	0.	1008.888	2.00	0.	0.000	0.2660	0.2885	0.1152														
2.00	0.10	27.	24.	1050.551	2.00	17.	0.060	0.2660	0.2885	0.1152														
2.00	0.30	97.	69.	1177.056	2.00	56.	0.203	0.2660	0.2892	0.1154														
2.00	0.50	164.	119.	1267.754	2.00	105.	0.392	0.2664	0.3352	0.1294														
2.00	0.60	200.	146.	1293.495	2.00	134.	0.502	0.2669	0.3978	0.1474														
2.00	0.70	239.	176.	1316.637	2.00	168.	0.629	0.2675	0.4682	0.1663														
2.00	0.80	285.	210.	1332.516	2.00	215.	0.799	0.2677	0.4900	0.1718														
2.00	0.90	370.	253.	1337.360	2.00	223.	0.826	0.2696	0.6955	0.2187														
2.00	0.95	386.	263.	1340.230	2.00	210.	0.775	0.2704	0.7895	0.2373														
1.70	0.00	0.	0.	1633.971	1.70	0.	0.000	0.2660	0.2885	0.1152														
1.70	0.10	26.	23.	1705.879	1.70	17.	0.062	0.2660	0.2885	0.1152														
1.70	0.30	93.	67.	1903.093	1.70	54.	0.202	0.2660	0.2887	0.1153														
1.70	0.50	154.	114.	2068.535	1.70	102.	0.391	0.2664	0.3214	0.1252														
1.70	0.60	188.	141.	2108.224	1.70	130.	0.498	0.2670	0.3732	0.1402														
1.70	0.70	226.	170.	2148.808	1.70	163.	0.625	0.2676	0.4319	0.1562														
1.70	0.80	269.	202.	2166.672	1.70	206.	0.783	0.2677	0.4483	0.1605														
1.70	0.90	324.	243.	2200.253	1.70	216.	0.821	0.2694	0.5730	0.1907														
1.70	0.95	358.	265.	2181.676	1.70	212.	0.809	0.2711	0.7294	0.2228														

Notes. The data presented in this table are: initial mass (Col. 1), initial rotation rate (Col. 2), initial equatorial velocity (Col. 3), mean equatorial velocity during the MS (Col. 4). For each burning phase, we also give the duration of the phase (Cols. 5, 12, and 19), the mass at the end of the phase (Cols. 6, 13, and 20), the equatorial velocity (Col. 7), or the rotation period at the end of the phase (Cols. 14, and 21), the ratio of the equatorial velocity to the critical one (Col. 8) or the ratio of the angular velocity to the critical one at the end of the burning phase (Cols. 15, and 22), the surface helium mass fraction (Cols. 9, 16, 23), the ratio N/C (Cols. 10, 17, and 24) and N/O at the end of the phase (Cols. 11, 18, and 25).

Table 3. Main parameters of A-B stars at $Z = 0.006 = Z_{\rm LMC}$.

				End of H-burning							End of He-burning							End of C-burning						
$M_{\rm ini}$	$\Omega/\Omega_{\rm crit,\,ini}$	$v_{\rm eq}$	$\bar{v}_{\rm MS}$	$\tau_{\rm H}$	M	$v_{\rm eq}$	$v_{\rm eq}/v_{\rm crit}$	$Y_{\rm surf}$	N/C	N/O	$\tau_{\rm He}$	M	$P_{\rm rot}$	$\Omega_{\rm S}/\Omega_{\rm C}$	$Y_{\rm surf}$	N/C	N/O	$\tau_{\rm C}$	M	$P_{\rm rot}$	$\Omega_{\rm S}/\Omega_{\rm C}$	$Y_{\rm surf}$	N/C	N/O
$M_\odot$		km s^{-1}		Myr	$M_\odot$	km s^{-1}			mass fract.		Myr	$M_\odot$	km s^{-1}			mass fract.		kyr	$M_\odot$	km s^{-1}			mass fract.	
15.00	0.00	0.	0.	11.097	14.87	0.	0.000	0.2559	0.2885	0.1152	1.338	14.00	–	–	0.2685	1.3634	0.3566	3.504	13.90	–	–	0.3214	2.7453	0.6739
15.00	0.10	48.	33.	11.786	14.85	22.	0.049	0.2559	0.2928	0.1165	1.403	13.51	$5.472 \cdot 10^5$	$5.194 \cdot 10^6$	0.2969	2.2371	0.5926	3.122	13.41	$8.667 \cdot 10^5$	$7.305 \cdot 10^8$	0.3318	3.2222	0.8165
15.00	0.30	149.	106.	12.889	14.81	91.	0.204	0.2611	0.9632	0.3011	1.320	13.61	$7.953 \cdot 10^4$	$1.680 \cdot 10^6$	0.3412	4.2953	0.8980	2.332	13.50	$1.475 \cdot 10^5$	$2.689 \cdot 10^8$	0.3647	5.3239	1.0507
15.00	0.50	252.	185.	13.409	14.80	168.	0.370	0.2776	2.7679	0.5921	1.286	13.92	$3.766 \cdot 10^4$	$1.143 \cdot 10^6$	0.3490	6.5843	1.0305	2.475	13.80	$6.487 \cdot 10^4$	$1.772 \cdot 10^8$	0.3845	8.8557	1.2540
15.00	0.60	289.	226.	13.547	14.80	211.	0.458	0.2864	4.2331	0.7202	1.307	13.89	$3.222 \cdot 10^4$	$1.125 \cdot 10^6$	0.3402	8.2676	1.0503	2.849	13.76	$5.534 \cdot 10^4$	$1.791 \cdot 10^8$	0.3885	11.8407	1.3410
15.00	0.70	369.	270.	13.696	14.79	252.	0.536	0.2957	6.4350	0.8399	1.399	13.96	$2.783 \cdot 10^4$	$1.166 \cdot 10^6$	0.3591	12.8962	1.2311	2.349	13.85	$4.668 \cdot 10^4$	$1.754 \cdot 10^8$	0.3959	16.9753	1.5184
15.00	0.80	417.	315.	14.481	14.76	282.	0.589	0.3176	11.7098	1.0271	1.397	13.76	$3.025 \cdot 10^4$	$1.393 \cdot 10^6$	0.3680	19.5376	1.3101	2.074	13.64	$4.716 \cdot 10^4$	$1.968 \cdot 10^8$	0.4242	28.5455	1.8231
15.00	0.90	524.	362.	15.753	14.69	302.	0.630	0.3622	25.2614	1.2928	1.237	12.53	$7.968 \cdot 10^4$	$3.651 \cdot 10^6$	0.4232	40.3338	1.6175	1.453	12.38	$9.421 \cdot 10^4$	$3.757 \cdot 10^8$	0.4697	51.9572	2.0796
15.00	0.95	587.	390.	16.133	14.68	308.	0.636	0.3742	32.4405	1.3712	1.211	12.33	$1.066 \cdot 10^5$	$4.979 \cdot 10^6$	0.4316	49.7553	1.6533	1.599	12.17	$1.095 \cdot 10^5$	$4.690 \cdot 10^8$	0.4707	58.6210	1.9853
12.00	0.00	0.	0.	15.310	11.95	0.	0.000	0.2559	0.2885	0.1152	1.976	10.95	–	–	0.2667	1.5412	0.3811	6.465	10.88	–	–	0.2977	2.4608	0.5905
12.00	0.10	44.	33.	16.277	11.95	24.	0.055	0.2559	0.2888	0.1153	1.942	10.76	$4.871 \cdot 10^5$	$5.427 \cdot 10^6$	0.2756	1.9693	0.5192	7.630	10.68	$8.494 \cdot 10^5$	$1.264 \cdot 10^9$	0.3060	2.8601	0.7254
12.00	0.30	131.	102.	17.783	11.93	95.	0.217	0.2584	0.7459	0.2469	1.822	10.39	$1.428 \cdot 10^5$	$3.447 \cdot 10^6$	0.3000	3.4505	0.7163	6.173	10.30	$2.397 \cdot 10^5$	$6.628 \cdot 10^8$	0.3293	4.5785	0.8818
12.00	0.50	242.	178.	18.395	11.93	177.	0.400	0.2699	2.3935	0.5259	1.910	11.42	$2.350 \cdot 10^4$	$8.443 \cdot 10^5$	0.3068	5.3803	0.8292	5.168	11.34	$4.826 \cdot 10^4$	$1.910 \cdot 10^8$	0.3499	7.7164	1.0572
12.00	0.60	275.	219.	18.572	11.93	221.	0.490	0.2779	3.9455	0.6631	2.046	11.47	$1.858 \cdot 10^4$	$7.837 \cdot 10^5$	0.3213	8.1782	0.9544	4.116	11.39	$4.067 \cdot 10^4$	$1.837 \cdot 10^8$	0.3579	10.9273	1.1534
12.00	0.70	330.	262.	18.664	11.93	267.	0.582	0.2861	6.4532	0.7875	2.065	11.33	$1.975 \cdot 10^4$	$9.419 \cdot 10^5$	0.3219	12.4816	1.0198	5.920	11.24	$3.295 \cdot 10^4$	$1.931 \cdot 10^8$	0.3569	15.8098	1.2025
12.00	0.80	423.	308.	18.758	11.93	318.	0.675	0.2939	10.4655	0.8913	2.291	11.33	$1.714 \cdot 10^4$	$9.974 \cdot 10^5$	0.3331	20.5658	1.1150	0.078	11.25	$2.889 \cdot 10^4$	$2.812 \cdot 10^7$	0.3592	24.2797	1.2414
12.00	0.90	510.	360.	21.313	11.90	365.	0.777	0.3409	29.6185	1.1881	1.872	10.98	$2.543 \cdot 10^4$	$1.547 \cdot 10^6$	0.3892	50.5192	1.4042	0.059	10.89	$3.432 \cdot 10^4$	$2.774 \cdot 10^7$	0.4114	56.7852	1.5159
12.00	0.95	569.	391.	22.249	11.88	378.	0.799	0.3638	44.9194	1.3331	1.802	11.07	$2.209 \cdot 10^4$	$1.317 \cdot 10^6$	0.4041	67.7565	1.5184	0.040	10.98	$3.258 \cdot 10^4$	$2.320 \cdot 10^7$	0.4299	77.6552	1.6540
9.00	0.00	0.	0.	25.992	8.99	0.	0.000	0.2559	0.2885	0.1152	3.363	8.65	–	–	0.2614	1.5134	0.3785	0.001	8.61	–	–	0.2736	1.8993	0.4749
9.00	0.10	45.	32.	27.333	8.99	25.	0.059	0.2559	0.2885	0.1152	3.304	8.73	$5.180 \cdot 10^4$	$6.417 \cdot 10^5$	0.2729	2.1345	0.5357	0.046	8.69	$1.589 \cdot 10^5$	$9.650 \cdot 10^7$	0.2773	2.3089	0.5711
9.00	0.30	123.	98.	29.932	8.99	94.	0.225	0.2570	0.5544	0.1958	3.168	8.70	$1.881 \cdot 10^4$	$5.128 \cdot 10^5$	0.2981	3.5358	0.7146	0.053	8.65	$5.740 \cdot 10^4$	$5.775 \cdot 10^7$	0.3004	3.7268	0.7339
9.00	0.50	228.	169.	30.861	8.99	175.	0.410	0.2649	1.9041	0.4538	3.242	8.74	$1.244 \cdot 10^4$	$5.072 \cdot 10^5$	0.3103	6.2920	0.8623	0.047	8.69	$3.279 \cdot 10^4$	$5.744 \cdot 10^7$	0.3146	6.6121	0.8869
9.00	0.60	279.	207.	31.091	8.99	218.	0.502	0.2713	3.2512	0.5922	3.355	8.80	$1.069 \cdot 10^4$	$5.174 \cdot 10^5$	0.3098	8.5053	0.9093	0.008	8.75	$2.615 \cdot 10^4$	$6.749 \cdot 10^7$	0.3196	9.5706	0.9622
9.00	0.70	331.	248.	31.183	8.99	265.	0.598	0.2782	5.4215	0.7187	3.749	8.91	$6.854 \cdot 10^3$	$3.879 \cdot 10^5$	0.3074	11.2245	0.9394	0.060	8.87	$1.911 \cdot 10^4$	$3.621 \cdot 10^7$	0.3213	13.8242	1.0176
9.00	0.80	392.	292.	31.292	8.99	318.	0.704	0.2852	8.8693	0.8277	3.788	8.94	$5.431 \cdot 10^3$	$3.597 \cdot 10^5$	0.3132	17.8575	1.0164	0.043	8.89	$1.509 \cdot 10^4$	$4.548 \cdot 10^7$	0.3274	22.0803	1.0901
9.00	0.90	465.	343.	34.282	8.99	393.	0.875	0.3093	21.1362	1.0484	3.282	8.92	$5.699 \cdot 10^3$	$3.973 \cdot 10^5$	0.3447	39.2807	1.2232	0.044	8.86	$1.367 \cdot 10^4$	$3.918 \cdot 10^7$	0.3565	46.2713	1.2773
9.00	0.95	528.	372.	35.516	8.98	394.	0.858	0.3296	33.6904	1.1950	3.504	8.90	$6.221 \cdot 10^3$	$4.743 \cdot 10^5$	0.3678	58.1684	1.3719	0.057	8.84	$1.436 \cdot 10^4$	$3.451 \cdot 10^7$	0.3808	67.9385	1.4335
7.00	0.00	0.	0.	41.395	7.00	0.	0.000	0.2559	0.2885	0.1152	6.275	6.89	–	–	0.2587	1.3783	0.3438							
7.00	0.10	43.	31.	43.205	7.00	25.	0.060	0.2559	0.2885	0.1152	6.197	6.90	$2.107 \cdot 10^4$	$3.040 \cdot 10^5$	0.2689	1.8983	0.4763							
7.00	0.30	129.	93.	47.420	7.00	90.	0.223	0.2564	0.4296	0.1594	5.752	6.87	$9.951 \cdot 10^3$	$3.235 \cdot 10^5$	0.2903	3.0605	0.6488							
7.00	0.50	217.	160.	48.956	7.00	166.	0.407	0.2613	1.3475	0.3665	5.903	6.88	$5.753 \cdot 10^3$	$2.729 \cdot 10^5$	0.3020	5.2802	0.7972							
7.00	0.60	260.	197.	49.298	7.00	207.	0.499	0.2661	2.2769	0.4948	6.177	6.90	$4.467 \cdot 10^3$	$2.537 \cdot 10^5$	0.3059	7.2685	0.8655							
7.00	0.70	320.	235.	49.513	7.00	252.	0.597	0.2716	3.6906	0.6153	6.791	6.91	$3.653 \cdot 10^3$	$2.422 \cdot 10^5$	0.3093	10.3670	0.9271							
7.00	0.80	370.	278.	49.821	7.00	304.	0.707	0.2780	5.8915	0.7285	7.209	6.93	$2.956 \cdot 10^3$	$2.222 \cdot 10^5$	0.3113	14.6980	0.9800							
7.00	0.90	447.	327.	50.087	7.00	377.	0.859	0.2841	9.1889	0.8396	7.361	6.94	$2.541 \cdot 10^3$	$2.187 \cdot 10^5$	0.3101	19.1856	1.0263							
7.00	0.95	496.	355.	50.622	7.00	399.	0.903	0.2898	12.0638	0.9159	7.729	6.98	$2.594 \cdot 10^3$	$2.244 \cdot 10^5$	0.3155	23.9778	1.0888							
5.00	0.00	0.	0.	83.169	5.00	0.	0.000	0.2559	0.2885	0.1152	15.908	4.95	–	–	0.2582	1.3024	0.3256							
5.00	0.10	36.	29.	86.831	5.00	23.	0.060	0.2559	0.2885	0.1152	16.797	4.94	$7.229 \cdot 10^3$	$1.199 \cdot 10^5$	0.2660	1.6548	0.4236							
5.00	0.30	109.	87.	95.898	5.00	82.	0.218	0.2561	0.3495	0.1347	14.949	4.93	$3.656 \cdot 10^3$	$1.426 \cdot 10^5$	0.2854	2.6598	0.5938							
5.00	0.50	187.	150.	99.280	5.00	152.	0.401	0.2588	0.8924	0.2773	15.334	4.93	$2.292 \cdot 10^3$	$1.291 \cdot 10^5$	0.2958	4.2339	0.7274							
5.00	0.60	245.	184.	100.247	5.00	190.	0.496	0.2617	1.4211	0.3773	16.006	4.93	$1.823 \cdot 10^3$	$1.192 \cdot 10^5$	0.2999	5.3840	0.7876							
5.00	0.70	276.	220.	100.700	5.00	232.	0.598	0.2653	2.1711	0.4758	16.435	4.94	$1.461 \cdot 10^3$	$1.141 \cdot 10^5$	0.3024	6.9844	0.8332							
5.00	0.80	360.	261.	101.328	5.00	283.	0.718	0.2695	3.2562	0.5746	16.528	4.95	$1.073 \cdot 10^3$	$9.861 \cdot 10^4$	0.3070	9.8091	0.8985							
5.00	0.90	421.	307.	101.391	5.00	357.	0.890	0.2716	4.2426	0.6364	17.932	4.95	$8.869 \cdot 10^2$	$9.326 \cdot 10^4$	0.3072	12.7927	0.9371							
5.00	0.95	438.	334.	101.879	5.00	358.	0.888	0.2728	4.6592	0.6626	18.136	4.95	$8.985 \cdot 10^2$	$1.009 \cdot 10^5$	0.3070	14.3721	0.9593							
4.00	0.00	0.	0.	137.775	4.00	0.	0.000	0.2559	0.2885	0.1152	33.275	3.96	–	–	0.2623	1.4460	0.3596							
4.00	0.10	38.	28.	143.820	4.00	22.	0.059	0.2559	0.2885	0.1152	33.000	3.96	$3.350 \cdot 10^3$	$6.122 \cdot 10^4$	0.2682	1.6244	0.4137							
4.00	0.30	115.	83.	159.264	4.00	76.	0.215	0.2560	0.3208	0.1255	29.021	3.95	$1.572 \cdot 10^3$	$6.698 \cdot 10^4$	0.2874	2.5587	0.5779							
4.00	0.50	196.	143.	165.639	4.00	141.	0.396	0.2576	0.6796	0.2261	28.500	3.95	$9.016 \cdot 10^2$	$5.691 \cdot 10^4$	0.2970	3.8659	0.6970							
4.00	0.60	240.	176.	167.463	4.00	177.	0.494	0.2598	1.0704	0.3111	28.864	3.95	$7.179 \cdot 10^2$	$5.405 \cdot 10^4$	0.3001	4.8095	0.7495							
4.00	0.70	282.	211.	168.745	4.00	218.	0.604	0.2624	1.5673	0.3931	30.519	3.96	$6.436 \cdot 10^2$	$5.558 \cdot 10^4$	0.3030	5.9616	0.7940							
4.00	0.80	332.	249.	169.522	4.00	268.	0.732	0.2651	2.1962	0.4704	32.690	3.96	$5.762 \cdot 10^2$	$5.656 \cdot 10^4$	0.3067	7.8889	0.8485							
4.00	0.90	403.	295.	170.134	4.00	308.	0.830	0.2650	2.4387	0.4900	33.696	3.96	$4.728 \cdot 10^2$	$5.373 \cdot 10^4$	0.3089	10.4870	0.8932							
4.00	0.95	471.	322.	170.473	4.00	302.	0.810	0.2692	3.3039	0.5652	35.440	3.96	$4.810 \cdot 10^2$	$5.792 \cdot 10^4$	0.3085	11.7103	0.9063							
3.00	0.00	0.	0.	276.224	3.00	0.	0.000	0.2559	0.2885	0.1152	91.745	2.98	–	–	0.2730	1.6582	0.4072							
3.00	0.10	32.	26.	286.111	3.00	19.	0.058	0.2559	0.2885	0.1152	94.742	2.98	$1.258 \cdot 10^3$	$2.620 \cdot 10^4$	0.2767	1.7177	0.4283							
3.00	0.30	110.	78.	319.604	3.00	67.	0.210	0.2560	0.3042	0.1201	75.969	2.97	$5.556 \cdot 10^2$	$2.764 \cdot 10^4$	0.2972	2.6327	0.5873							
3.00	0.50	185.	135.	335.387	3.00	126.	0.394	0.2571	0.5369	0.1880	77.623	2.97	$4.049 \cdot 10^2$	$2.891 \cdot 10^4$	0.3054	3.6971	0.6851							
3.00	0.60	206.	166.	339.749	3.00	160.	0.497	0.2585	0.7813	0.2470	76.023	2.97	$3.232 \cdot 10^2$	$2.627 \cdot 10^4$	0.3086	4.4546	0.7298							
3.00	0.70	271.	199.	342.777	3.00	198.	0.607	0.2605	1.1276	0.3153	80.224	2.97	$3.342 \cdot 10^2$	$3.161 \cdot 10^4$	0.3100	5.3672	0.7647							
3.00	0.80	295.	236.	345.579	3.00	247.	0.751	0.2618	1.4397	0.3635	81.176	2.97	$2.836 \cdot 10^2$	$3.028 \cdot 10^4$	0.3131	6.6684	0.8059							
3.00	0.90	389.	281.	347.185	3.00	278.	0.830	0.2628	1.6815	0.3960	77.906	2.97	$2.043 \cdot 10^2$	$2.637 \cdot 10^4$	0.3140	8.4523	0.8444							
3.00	0.95	436.	307.	348.099	3.00	272.	0.810	0.2668	2.4237	0.4789	83.829	2.97	$1.985 \cdot 10^2$	$2.562 \cdot 10^4$	0.3157	9.5293	0.8633							
2.50	0.00	0.	0.	440.910	2.50	0.	0.000	0.2559	0.2885	0.1152	175.074	2.48	–	–	0.2757	1.6266	0.3952							
2.50	0.10	34.	25.	457.083	2.50	19.	0.059	0.2559	0.2885	0.1152	181.413	2.48	$8.377 \cdot 10^2$	$1.934 \cdot 10^4$	0.2792	1.6110	0.4025							
2.50	0.30	105.	75.	514.068	2.50	64.	0.208	0.2559	0.2989	0.1184	159.866	2.48	$3.598 \cdot 10^2$	$1.975 \cdot 10^4$	0.3003	2.5368	0.5645							
2.50	0.50	178.	130.	541.514	2.50	121.	0.395	0.2569	0.4771	0.1707	152.438	2.48	$2.381 \cdot 10^2$	$1.854 \cdot 10^4$	0.3098	3.5255	0.6559							
2.50	0.60	198.	160.	549.620	2.50	153.	0.498	0.2582	0.6761	0.2205	141.426	2.48	$1.739 \cdot 10^2$	$1.673 \cdot 10^4$	0.3127	4.1915	0.6971							
2.50	0.70	236.	192.	555.058	2.50	191.	0.614	0.2597	0.9429	0.2759	155.846	2.48	$1.744 \cdot 10^2$	$1.787 \cdot 10^4$	0.3152	5.1187	0.7370							
2.50	0.80	309.	228.	559.658	2.50	240.	0.764	0.2608	1.1566	0.3122	154.259	2.48	$1.494 \cdot 10^2$	$1.787 \cdot 10^4$	0.3153	6.0331	0.7590							
2.50	0.90	372.	271.	563.501	2.50	263.	0.827	0.2626	1.4650	0.3591	154.899	2.48	$1.299 \cdot 10^2$	$1.792 \cdot 10^4$	0.3167	7.3960	0.7946							
2.50	0.95	418.	298.	565.360	2.50	265.	0.831	0.2663	2.1052	0.4356	153.547	2.48	$1.332 \cdot 10^2$	$1.914 \cdot 10^4$	0.3190	8.3689	0.8175							
2.00	0.00	0.	0.	805.801	2.00	0.	0.000	0.2559	0.2885	0.1152														
2.00	0.10	29.	25.	839.531	2.00	19.	0.061	0.2559	0.2885	0.1152														
2.00	0.30	88.	73.	947.948	2.00	63.	0.214	0.2560	0.2951	0.1172														
2.00	0.50	150.	127.	1007.382	2.00	120.	0.412	0.2571	0.4409	0.1596														
2.00	0.60	213.	156.	1022.614	2.00	152.	0.519	0.2584	0.5977	0.1985														
2.00	0.70	253.	188.	1034.130	2.00	191.	0.647	0.2600	0.7980	0.2414														
2.00	0.80	309.	224.	1045.843	2.00	237.	0.795	0.2605	0.9126	0.2611														
2.00	0.90	366.	269.	1048.349	2.00	243.	0.805	0.2645	1.4343	0.3397														
2.00	0.95	426.	292.	1054.389	2.00	246.	0.817	0.2671	1.8486	0.3842														
1.70	0.00	0.	0.	1284.504	1.70	0.	0.000	0.2559	0.2885	0.1152														
1.70	0.10	27.	25.	1344.255	1.70	19.	0.063	0.2559	0.2885	0.1152														
1.70	0.30	83.	71.	1519.179	1.70	62.	0.215	0.2560	0.2920	0.1163														
1.70	0.50	163.	123.	1616.978	1.70	117.	0.413	0.2573	0.4062	0.1494														
1.70	0.60	199.	152.	1646.526	1.70	149.	0.525	0.2587	0.5352	0.1820														
1.70	0.70	239.	183.	1666.675	1.70	188.	0.655	0.2604	0.6918	0.2164														
1.70	0.80	287.	219.	1679.739	1.70	236.	0.811	0.2609	0.7790	0.2330														
1.70	0.90	342.	262.	1677.683	1.70	241.	0.817	0.2657	1.2567	0.3066														
1.70	0.95	371.	284.	1695.775	1.70	238.	0.812	0.2687	1.5883	0.3451														

Notes. Same as in Table 2.

Table 4. Main parameters of A-B stars at $Z = 0.002 = Z_{\rm SMC}$.

				End of H-burning							End of He-burning							End of C-burning						
$M_{\rm ini}$	$\Omega/\Omega_{\rm crit,\,ini}$	$v_{\rm eq}$	$\bar{v}_{\rm MS}$	$\tau_{\rm H}$	M	$v_{\rm eq}$	$v_{\rm eq}/v_{\rm crit}$	$Y_{\rm surf}$	N/C	N/O	$\tau_{\rm He}$	M	$P_{\rm rot}$	$\Omega_{\rm c}/\Omega_{\rm s}$	$Y_{\rm surf}$	N/C	N/O	$\tau_{\rm C}$	M	$P_{\rm rot}$	$\Omega_{\rm c}/\Omega_{\rm s}$	$Y_{\rm surf}$	N/C	N/O
$M_\odot$		km s^{-1}		Myr	$M_\odot$	km s^{-1}			mass fract.		Myr	$M_\odot$	day			mass fract.		kyr	$M_\odot$	day			mass fract.	
15.00	0.00	0.	0.	10.996	14.92	0.	0.000	0.2509	0.2885	0.1152	1.363	14.69	–	–	0.2538	1.0804	0.2851	2.143	14.60	–	–	0.3078	2.6821	0.6375
15.00	0.10	47.	36.	11.712	14.91	26.	0.053	0.2509	0.2955	0.1174	1.366	14.72	$9.711 \cdot 10^4$	$9.187 \cdot 10^5$	0.2730	1.9569	0.5093	2.483	14.61	$1.741 \cdot 10^5$	$1.312 \cdot 10^8$	0.3174	3.4360	0.8187
15.00	0.30	156.	113.	12.749	14.89	104.	0.218	0.2577	1.4288	0.3972	1.277	14.76	$5.125 \cdot 10^3$	$1.142 \cdot 10^5$	0.2592	1.5687	0.4238	2.510	14.65	$5.300 \cdot 10^4$	$1.032 \cdot 10^8$	0.3562	6.7244	1.1727
15.00	0.50	264.	197.	13.174	14.88	191.	0.391	0.2757	4.5795	0.7518	1.323	14.48	$2.390 \cdot 10^4$	$7.992 \cdot 10^5$	0.3104	8.3919	1.0121	2.398	14.35	$3.577 \cdot 10^4$	$1.037 \cdot 10^8$	0.3762	13.5690	1.5163
15.00	0.60	322.	241.	13.298	14.88	236.	0.472	0.2860	7.8167	0.9067	1.359	14.77	$5.927 \cdot 10^2$	$2.293 \cdot 10^4$	0.2882	8.1847	0.9242	2.831	14.68	$2.549 \cdot 10^4$	$9.562 \cdot 10^7$	0.3937	23.9491	1.9992
15.00	0.70	386.	285.	14.821	14.84	290.	0.578	0.3287	21.7949	1.2305	1.294	14.35	$2.196 \cdot 10^4$	$9.577 \cdot 10^5$	0.3615	31.6109	1.3935	1.117	14.21	$3.076 \cdot 10^4$	$1.105 \cdot 10^8$	0.4302	47.4717	2.1263
15.00	0.80	460.	335.	15.594	14.82	334.	0.647	0.3637	46.3328	1.4467	1.224	14.15	$2.565 \cdot 10^4$	$1.263 \cdot 10^6$	0.4028	66.8905	1.6397	1.577	13.98	$3.197 \cdot 10^4$	$1.409 \cdot 10^8$	0.4481	77.6722	2.0158
15.00	0.90	552.	391.	17.001	14.77	387.	0.751	0.4167	97.5790	1.7815	1.056	13.80	$3.466 \cdot 10^4$	$1.654 \cdot 10^6$	0.4484	121.0607	1.9557	0.035	13.62	$4.258 \cdot 10^4$	$1.608 \cdot 10^7$	0.4817	123.2309	2.2346
15.00	0.95	580.	424.	16.820	14.77	363.	0.699	0.4126	105.3703	1.8105	1.118	14.24	$2.044 \cdot 10^4$	$1.026 \cdot 10^6$	0.4436	128.1636	1.9873	1.136	14.05	$2.966 \cdot 10^4$	$1.244 \cdot 10^8$	0.4685	133.5483	2.1527
12.00	0.00	0.	0.	15.100	11.97	0.	0.000	0.2509	0.2885	0.1152	1.852	11.91	–	–	0.2509	0.9303	0.2531	6.643	11.83	–	–	0.2900	2.4466	0.5674
12.00	0.10	49.	35.	16.047	11.96	26.	0.056	0.2509	0.2895	0.1155	1.870	11.91	$4.175 \cdot 10^4$	$4.509 \cdot 10^5$	0.2549	1.0492	0.3146	6.556	11.83	$1.356 \cdot 10^5$	$1.619 \cdot 10^8$	0.2928	3.0635	0.7176
12.00	0.30	137.	108.	17.495	11.96	101.	0.218	0.2549	1.1774	0.3417	1.776	11.87	$1.364 \cdot 10^4$	$3.398 \cdot 10^5$	0.2680	2.4340	0.5550	5.300	11.79	$4.355 \cdot 10^4$	$1.176 \cdot 10^8$	0.3263	5.6993	0.9809
12.00	0.50	254.	187.	18.006	11.95	188.	0.395	0.2706	4.4735	0.7233	1.841	11.89	$5.165 \cdot 10^3$	$1.925 \cdot 10^5$	0.2733	4.8518	0.7520	6.206	11.80	$2.328 \cdot 10^4$	$1.093 \cdot 10^8$	0.3488	12.9178	1.2772
12.00	0.60	309.	229.	18.156	11.95	233.	0.479	0.2806	8.0964	0.8806	2.073	11.83	$1.213 \cdot 10^4$	$5.541 \cdot 10^5$	0.3067	13.9188	1.0705	3.123	11.75	$2.145 \cdot 10^4$	$1.042 \cdot 10^8$	0.3525	20.3117	1.3710
12.00	0.70	371.	274.	18.238	11.96	282.	0.566	0.2892	14.4001	1.0083	2.149	11.84	$1.088 \cdot 10^4$	$5.782 \cdot 10^5$	0.3188	25.9367	1.1933	0.060	11.76	$1.554 \cdot 10^4$	$1.570 \cdot 10^7$	0.3404	30.9826	1.3153
12.00	0.80	443.	320.	20.621	11.94	341.	0.681	0.3373	45.9913	1.3230	1.888	11.84	$5.328 \cdot 10^3$	$2.968 \cdot 10^5$	0.3512	54.3409	1.3887	0.072	11.75	$1.651 \cdot 10^4$	$1.154 \cdot 10^7$	0.3948	81.7906	1.6103
12.00	0.90	534.	377.	21.813	11.92	394.	0.791	0.3753	97.2772	1.5771	1.624	11.83	$1.506 \cdot 10^3$	$9.275 \cdot 10^4$	0.3814	102.3901	1.6073	0.072	11.73	$1.563 \cdot 10^4$	$1.134 \cdot 10^7$	0.4240	139.1205	1.8305
12.00	0.95	599.	410.	22.266	11.91	426.	0.837	0.3957	132.0904	1.7541	1.645	11.81	$1.157 \cdot 10^3$	$7.235 \cdot 10^4$	0.4008	136.4635	1.7816	0.068	11.71	$1.564 \cdot 10^4$	$1.081 \cdot 10^7$	0.4392	164.1779	2.0035
9.00	0.00	0.	0.	25.471	8.99	0.	0.000	0.2509	0.2885	0.1152	2.999	8.89	–	–	0.2510	1.2200	0.2935	0.047	8.85	–	–	0.2623	2.0719	0.4711
9.00	0.10	44.	34.	26.901	8.99	26.	0.058	0.2509	0.2886	0.1152	3.123	8.87	$3.864 \cdot 10^3$	$4.836 \cdot 10^4$	0.2579	1.8148	0.4497	0.060	8.83	$9.448 \cdot 10^4$	$4.645 \cdot 10^7$	0.2734	2.6099	0.6068
9.00	0.30	143.	102.	29.320	8.99	98.	0.219	0.2533	0.9461	0.2916	2.874	8.90	$1.818 \cdot 10^3$	$5.098 \cdot 10^4$	0.2761	3.4263	0.6705	0.063	8.85	$3.496 \cdot 10^4$	$3.133 \cdot 10^7$	0.2945	4.7781	0.8208
9.00	0.50	241.	177.	30.090	8.99	180.	0.392	0.2659	3.9935	0.6728	3.170	8.97	$2.075 \cdot 10^3$	$8.907 \cdot 10^4$	0.2666	4.1190	0.6828	0.061	8.92	$1.941 \cdot 10^4$	$2.626 \cdot 10^7$	0.3065	10.6774	1.0264
9.00	0.60	294.	216.	30.251	8.99	223.	0.476	0.2746	7.5906	0.8446	3.280	8.98	$3.809 \cdot 10^2$	$1.919 \cdot 10^4$	0.2755	7.8088	0.8533	0.053	8.93	$1.489 \cdot 10^4$	$2.626 \cdot 10^7$	0.3139	18.0809	1.1371
9.00	0.70	326.	258.	30.364	8.99	269.	0.562	0.2828	14.1322	0.9733	3.547	8.98	$4.940 \cdot 10^2$	$3.003 \cdot 10^4$	0.2840	14.6087	0.9823	0.054	8.93	$1.251 \cdot 10^4$	$2.903 \cdot 10^7$	0.3223	32.4416	1.2325
9.00	0.80	421.	305.	30.791	8.99	315.	0.647	0.2928	27.1413	1.1088	3.916	8.98	$1.941 \cdot 10^2$	$1.393 \cdot 10^4$	0.2944	28.2893	1.1193	0.062	8.93	$1.096 \cdot 10^4$	$2.781 \cdot 10^7$	0.3338	58.3898	1.3397
9.00	0.90	507.	356.	36.377	8.99	420.	0.859	0.3577	105.3567	1.5778	3.003	8.96	$2.802 \cdot 10^2$	$2.103 \cdot 10^4$	0.3618	109.8773	1.5986	0.069	8.90	$1.115 \cdot 10^4$	$2.207 \cdot 10^7$	0.4021	156.6746	1.8131
9.00	0.95	564.	387.	37.256	8.98	430.	0.878	0.3804	146.9191	1.7473	2.821	8.95	$1.761 \cdot 10^2$	$1.356 \cdot 10^4$	0.3838	150.6317	1.7659	0.076	8.89	$1.064 \cdot 10^4$	$2.167 \cdot 10^7$	0.4219	187.4874	1.9825
7.00	0.00	0.	0.	39.945	7.00	0.	0.000	0.2509	0.2885	0.1152	5.570	6.94	–	–	0.2511	1.0737	0.2745							
7.00	0.10	42.	33.	41.842	7.00	26.	0.059	0.2509	0.2885	0.1152	5.705	6.93	$7.550 \cdot 10^3$	$1.081 \cdot 10^5$	0.2554	1.5427	0.3989							
7.00	0.30	134.	97.	45.541	7.00	94.	0.217	0.2522	0.7231	0.2395	5.151	6.93	$3.517 \cdot 10^3$	$1.130 \cdot 10^5$	0.2702	2.9180	0.6109							
7.00	0.50	230.	168.	46.821	7.00	171.	0.388	0.2615	3.0065	0.5893	5.565	6.94	$3.677 \cdot 10^2$	$1.780 \cdot 10^4$	0.2834	6.4559	0.8439							
7.00	0.60	272.	206.	46.961	7.00	212.	0.471	0.2686	5.5828	0.7536	5.586	6.96	$4.894 \cdot 10^2$	$2.888 \cdot 10^4$	0.2699	5.8510	0.7679							
7.00	0.70	337.	246.	47.123	7.00	255.	0.554	0.2761	10.1154	0.8910	6.005	7.00	$1.639 \cdot 10^2$	$1.144 \cdot 10^4$	0.2768	10.3426	0.8971							
7.00	0.80	392.	290.	47.473	7.00	303.	0.646	0.2841	18.1129	1.0220	6.330	7.00	$1.592 \cdot 10^2$	$1.311 \cdot 10^4$	0.2850	18.6923	1.0297							
7.00	0.90	466.	339.	51.775	7.00	357.	0.763	0.3103	46.8616	1.2846	5.889	6.99	$1.790 \cdot 10^2$	$1.724 \cdot 10^4$	0.3123	48.6833	1.2958							
7.00	0.95	515.	365.	56.509	7.00	413.	0.879	0.3450	93.7738	1.5255	5.101	6.99	$1.665 \cdot 10^2$	$1.608 \cdot 10^4$	0.3485	98.0867	1.5439							
5.00	0.00	0.	0.	77.356	5.00	0.	0.000	0.2509	0.2885	0.1152	13.652	4.96	–	–	0.2513	1.0048	0.2649							
5.00	0.10	42.	31.	81.192	5.00	24.	0.059	0.2509	0.2885	0.1152	13.806	4.96	$4.459 \cdot 10^3$	$7.541 \cdot 10^4$	0.2541	1.3504	0.3563							
5.00	0.30	126.	91.	89.006	5.00	87.	0.214	0.2516	0.5257	0.1871	12.641	4.94	$3.364 \cdot 10^3$	$1.241 \cdot 10^5$	0.2664	2.4307	0.5460							
5.00	0.50	217.	158.	91.541	5.00	159.	0.384	0.2576	1.9886	0.4722	12.905	4.95	$1.789 \cdot 10^3$	$1.034 \cdot 10^5$	0.2793	5.0756	0.7719							
5.00	0.60	265.	193.	92.138	5.00	197.	0.469	0.2631	3.5988	0.6380	13.190	4.96	$8.992 \cdot 10^2$	$6.298 \cdot 10^4$	0.2825	7.2449	0.8603							
5.00	0.70	291.	231.	92.364	5.00	238.	0.555	0.2694	6.2436	0.7800	13.569	4.96	$4.086 \cdot 10^2$	$3.426 \cdot 10^4$	0.2856	10.7309	0.9369							
5.00	0.80	378.	272.	92.857	5.00	283.	0.646	0.2765	10.7368	0.9099	14.608	4.96	$3.001 \cdot 10^2$	$2.910 \cdot 10^4$	0.2860	14.7615	0.9925							
5.00	0.90	416.	319.	94.149	5.00	334.	0.751	0.2847	18.3610	1.0419	14.720	5.00	$3.887 \cdot 10^2$	$4.374 \cdot 10^4$	0.2868	19.7208	1.0590							
5.00	0.95	516.	346.	95.799	5.00	378.	0.853	0.2899	24.3400	1.1364	14.362	5.00	$2.397 \cdot 10^2$	$2.973 \cdot 10^4$	0.2925	26.5232	1.1567							
4.00	0.00	0.	0.	124.375	4.00	0.	0.000	0.2509	0.2885	0.1152	26.143	3.97	–	–	0.2519	1.1545	0.2856							
4.00	0.10	36.	30.	130.376	4.00	23.	0.059	0.2509	0.2885	0.1152	26.390	3.96	$3.782 \cdot 10^3$	$6.906 \cdot 10^4$	0.2547	1.4183	0.3604							
4.00	0.30	111.	88.	143.570	4.00	82.	0.213	0.2513	0.4394	0.1616	23.433	3.95	$2.055 \cdot 10^3$	$8.531 \cdot 10^4$	0.2683	2.4789	0.5457							
4.00	0.50	189.	151.	148.207	4.00	150.	0.383	0.2557	1.5026	0.3932	22.925	3.96	$1.046 \cdot 10^3$	$6.835 \cdot 10^4$	0.2793	4.5882	0.7309							
4.00	0.60	233.	185.	148.916	4.00	188.	0.471	0.2599	2.6201	0.5372	24.508	3.96	$7.743 \cdot 10^2$	$5.883 \cdot 10^4$	0.2839	6.5644	0.8218							
4.00	0.70	295.	222.	149.487	4.00	226.	0.559	0.2653	4.4463	0.6793	25.396	3.96	$6.487 \cdot 10^2$	$5.837 \cdot 10^4$	0.2873	9.4450	0.9018							
4.00	0.80	333.	262.	150.071	4.00	271.	0.658	0.2710	7.2511	0.7918	25.366	3.97	$5.285 \cdot 10^2$	$5.723 \cdot 10^4$	0.2895	13.3764	0.9542							
4.00	0.90	425.	307.	151.278	4.00	323.	0.769	0.2779	12.0312	0.9301	26.664	3.97	$4.426 \cdot 10^2$	$5.567 \cdot 10^4$	0.2911	18.6611	1.0381							
4.00	0.95	487.	333.	152.800	4.00	376.	0.895	0.2812	14.8199	0.9692	27.807	3.96	$5.956 \cdot 10^2$	$7.748 \cdot 10^4$	0.2926	21.8880	1.0603							
3.00	0.00	0.	0.	240.308	3.00	0.	0.000	0.2509	0.2885	0.1152	63.990	2.97	–	–	0.2549	1.4165	0.3226							
3.00	0.10	38.	28.	249.120	3.00	22.	0.059	0.2509	0.2885	0.1152	61.145	2.97	$1.699 \cdot 10^3$	$3.654 \cdot 10^4$	0.2596	1.6139	0.3891							
3.00	0.30	104.	83.	277.567	3.00	76.	0.211	0.2512	0.3804	0.1440	54.157	2.96	$7.695 \cdot 10^2$	$3.771 \cdot 10^4$	0.2762	2.8641	0.5907							
3.00	0.50	197.	144.	288.299	3.00	139.	0.386	0.2546	1.1508	0.3291	54.555	2.96	$5.277 \cdot 10^2$	$3.858 \cdot 10^4$	0.2867	4.9278	0.7500							
3.00	0.60	240.	176.	290.221	3.00	173.	0.477	0.2576	1.8597	0.4334	57.072	2.96	$4.092 \cdot 10^2$	$3.531 \cdot 10^4$	0.2911	6.5391	0.7993							
3.00	0.70	288.	211.	292.264	3.00	210.	0.569	0.2620	3.0208	0.5507	60.437	2.96	$3.667 \cdot 10^2$	$3.737 \cdot 10^4$	0.2957	9.3463	0.8699							
3.00	0.80	342.	249.	293.620	3.00	253.	0.675	0.2668	4.7717	0.6592	60.804	2.96	$3.261 \cdot 10^2$	$3.909 \cdot 10^4$	0.2985	13.2479	0.9255							
3.00	0.90	412.	293.	294.880	3.00	310.	0.812	0.2712	7.1344	0.7499	64.448	2.96	$3.114 \cdot 10^2$	$4.377 \cdot 10^4$	0.3011	18.9509	0.9803							
3.00	0.95	420.	319.	296.847	3.00	313.	0.813	0.2715	7.6469	0.7734	65.639	2.96	$2.990 \cdot 10^2$	$4.375 \cdot 10^4$	0.3018	21.9796	1.0155							
2.50	0.00	0.	0.	374.191	2.50	0.	0.000	0.2509	0.2885	0.1152	114.955	2.48	–	–	0.2648	1.7337	0.3915							
2.50	0.10	34.	28.	388.262	2.50	21.	0.059	0.2509	0.2885	0.1152	119.687	2.47	$1.206 \cdot 10^3$	$2.575 \cdot 10^4$	0.2689	1.7836	0.4167							
2.50	0.30	100.	80.	436.691	2.50	72.	0.212	0.2512	0.3527	0.1351	104.896	2.47	$5.423 \cdot 10^2$	$2.831 \cdot 10^4$	0.2876	3.0701	0.6064							
2.50	0.50	172.	139.	453.569	2.50	133.	0.389	0.2542	0.9369	0.2794	97.722	2.47	$3.093 \cdot 10^2$	$2.553 \cdot 10^4$	0.2962	4.9999	0.7310							
2.50	0.60	230.	171.	457.950	2.50	167.	0.483	0.2571	1.5252	0.3768	98.247	2.47	$2.309 \cdot 10^2$	$2.252 \cdot 10^4$	0.3003	6.5559	0.7849							
2.50	0.70	253.	204.	460.889	2.50	205.	0.584	0.2608	2.4339	0.4749	108.008	2.47	$2.142 \cdot 10^2$	$2.424 \cdot 10^4$	0.3016	8.9037	0.8219							
2.50	0.80	300.	242.	462.715	2.50	249.	0.694	0.2651	3.8026	0.5762	115.112	2.46	$2.363 \cdot 10^2$	$3.002 \cdot 10^4$	0.3053	12.9695	0.8859							
2.50	0.90	395.	285.	466.427	2.50	300.	0.817	0.2682	5.1003	0.6395	115.288	2.47	$1.936 \cdot 10^2$	$2.918 \cdot 10^4$	0.3084	18.6595	0.9375							
2.50	0.95	400.	310.	468.888	2.50	311.	0.841	0.2695	5.7329	0.6636	112.967	2.47	$1.663 \cdot 10^2$	$2.674 \cdot 10^4$	0.3095	22.3530	0.9596							
2.00	0.00	0.	0.	667.029	2.00	0.	0.000	0.2509	0.2885	0.1152														
2.00	0.10	36.	27.	696.663	2.00	21.	0.062	0.2509	0.2885	0.1152														
2.00	0.30	112.	79.	790.716	2.00	72.	0.221	0.2512	0.3357	0.1297	205.165	1.97	$3.040 \cdot 10^2$	$1.950 \cdot 10^4$	0.2923	2.7512	0.5414							
2.00	0.50	183.	137.	825.594	2.00	134.	0.410	0.2547	0.8046	0.2451	194.067	1.97	$2.192 \cdot 10^2$	$2.047 \cdot 10^4$	0.3032	4.7208	0.6659							
2.00	0.60	223.	168.	834.069	2.00	169.	0.509	0.2579	1.2870	0.3249	198.499	1.97	$1.964 \cdot 10^2$	$1.867 \cdot 10^4$	0.3050	6.0322	0.7007							
2.00	0.70	268.	201.	837.165	2.00	209.	0.618	0.2616	1.9881	0.4031	0.000	1.98	$7.316 \cdot 10^2$	$3.162 \cdot 10^5$	0.3067	8.0971	0.7341							
2.00	0.80	322.	238.	843.153	2.00	259.	0.753	0.2656	2.9834	0.4785														
2.00	0.90	396.	282.	849.985	2.00	285.	0.810	0.2678	3.7471	0.5247														
2.00	0.95	409.	308.	871.563	2.00	298.	0.842	0.2753	5.6638	0.6399														
1.70	0.00	0.	0.	1053.592	1.70	0.	0.000	0.2509	0.2885	0.1152														
1.70	0.10	29.	27.	1101.952	1.70	21.	0.064	0.2509	0.2885	0.1152														
1.70	0.30	104.	77.	1253.898	1.70	71.	0.226	0.2513	0.3202	0.1248														
1.70	0.50	173.	133.	1313.265	1.70	134.	0.421	0.2552	0.6981	0.2181														
1.70	0.60	213.	164.	1337.826	1.70	169.	0.525	0.2592	1.1158	0.2898														
1.70	0.70	251.	196.	1337.166	1.70	210.	0.636	0.2636	1.6972	0.3599														
1.70	0.80	304.	232.	1538.864	1.70	265.	0.796	0.2809	4.0962	0.5528														
1.70	0.90	360.	267.	1444.859	1.70	303.	0.854	0.2802	5.2415	0.5449														
1.70	0.95	420.	298.	1701.731	1.70	272.	0.798	0.3111	12.7300	0.9124														

Notes. Same as in Table 2.